~~Variability~~ Climatology and variability of air mass transport from the boundary layer to the Asian monsoon anticyclone

Matthias Nützel[1], Sabine Brinkop[1], Martin Dameris[1], Hella Garny[1,2], Patrick Jöckel[1], Laura L. Pan[3], and Mijeong Park[3]

[1]Deutsches Zentrum für Luft- und Raumfahrt, Institut für Physik der Atmosphäre, Oberpfaffenhofen, Germany
[2]Meteorologisches Institut München, Ludwig-Maximilians-Universität München, Munich, Germany
[3]National Center for Atmospheric Research, Boulder, Colorado, USA

Correspondence: Matthias Nützel (matthias.nuetzel@dlr.de)

Abstract. Air masses within the Asian monsoon anticyclone (AMA) show anomalous signatures in various trace gases. In this study, we ~~analyze~~ investigate how air masses are transported from the planetary boundary layer (PBL) to the AMA via multiannual trajectory ~~anlyses. While previous studies analyzed the PBL to AMA transport mainly for individual monsoon seasons or particularperiods~~analyses. In particular, we focus on the climatological perspective and on the ~~interannual and~~
5 ~~intraseasonal variability.~~ intraseasonal and interannual variability. Further, we also discuss the relation of the interannual east–west displacements of the AMA with the PBL to AMA transport.

To this end we employ backward trajectories, which were computed ~~using reanalysis data. Based on these trajectories, we analyze air mass transport from the PBL to the AMA during~~ for 14 northern summer (June–August) ~~for 14 summer seasons seasons using reanalysis data~~. Further, we backtrack forward trajectories from a free-running chemistry-climate model (CCM)
10 simulation, which includes parametrized Lagrangian convection. The analysis of 30 monsoon seasons of this additional model data set helps us to carve out robust or sensitive features of PBL to AMA transport with respect to the employed model.

Results from both, the trajectory model and the Lagrangian CCM, emphasize the robustness of the three-dimensional transport pathways from the top of the PBL to the AMA. Air masses are transported upwards on the eastern side of the AMA and ~~are uplifted~~ circle upward within the full AMA domain above. ~~While this is in agreement with previous modelling studies, we~~
15 ~~refine the picture of the so-called "conduit" (Bergman et al., 2013). The contributions from the~~The contributions of different PBL source regions to AMA air are robust across the two models for the Tibetan Plateau (TP; 17% vs. 15%) and the West Pacific (around 12%)~~are similar in both model results~~. However, the contributions from the Indian subcontinent and South-East Asia are considerably larger in the Lagrangian CCM data, which might ~~point towards the importance~~ indicate an important role of convective transport for PBL to AMA transport for these regions.
20 The analysis of both model data sets highlights the interannual and intraseasonal variability with respect to PBL source regions of the AMA. ~~Additionally, we analyze the relation of the~~Although there are differences in the transport pathways, the interannual east–west displacement of the AMA - which we find to be related to the monsoon Hadley index - ~~to the transport behaviour and find that there are differences for "east" and "west years", the main transport characteristics, however, are comparable~~is not connected to considerable differences in the overall transport characteristics.
25 ~~Regarding the intraseasonal variability our trajectory model results show that~~

Our results from the trajectory model data reveal a strong intraseasonal signal in the transport from the PBL over the ~~Tibetan Plateau (TP)~~ TP to the AMA~~is weak~~: there is a weak contribution of TP air masses in early June (less than 4% of the AMA air masses), whereas in August ~~TP air masses contribute considerably~~ the contribution is considerable (roughly 24%). The evolution of the contribution from the TP is ~~supported by data from the Lagrangian CCM~~ consistent across the two modelling approaches and is related to the northward shift of the subtropical jet and the AMA during this period. This ~~result~~ finding may help to reconcile previous results and further highlights the need of taking the subseasonal (and interannual) variability of the AMA and associated transport into account.

1 Introduction

Strong precipitation during local summer is a typical criterion to define/identify monsoon regions (e.g. Wang et al., 2020). In the Asian summer monsoon (ASM) region, the heating related to the monsoon precipitation produces an anticyclone in the upper troposphere and lower stratosphere (UTLS) over Asia (e.g. Hoskins and Rodwell, 1995; Park et al., 2007; Siu and Bowman, 2019, and references therein), which is often referred to as Asian (summer) monsoon anticyclone (AMA; e.g. Randel and Park, 2006; Park et al., 2007; Siu and Bowman, 2020).

Due to fast uplift of polluted air masses in the ASM region (von Hobe et al., 2021) and confinement within the AMA (Legras and Bucci, 2020), trace gases such as carbon monoxide (CO) show a maximum within the anticyclone (e.g. Santee et al., 2017). Air masses that have reached the AMA or its edge can be further transported to the extratropical UTLS or the tropical stratosphere (e.g. Dethof et al., 1999; Randel et al., 2010; Vogel et al., 2014; Garny and Randel, 2016; Ploeger et al., 2017; Nützel et al., 2019; Vogel et al., 2019). In the stratosphere, these air masses might cause changes of the chemical and aerosol composition and hence affect the radiation budget (Randel et al., 2010). Thus, it is crucial to understand how trace gas anomalies within the AMA build up and how they are redistributed.

A first step towards answering these questions is to analyze the transport properties of air masses from the top of the planetary boundary layer (PBL) to the AMA. This topic has been investigated in a couple of previous trajectory-based studies, e.g. by Bergman et al. (2013), Heath and Fuelberg (2014), Vogel et al. (2015), Fan et al. (2017), Vogel et al. (2019), Bucci et al. (2020) and Legras and Bucci (2020), sometimes with a focus on transport to the UTLS in the ASM region in general. All of these studies focus on individual important aspects regarding the transport to the AMA or UTLS in the ASM region.

As an example, Bergman et al. (2013) found a favourable region of upward transport on the eastern side of the AMA and coined the term of the so called conduit. Further, they calculated sensitivities with respect to the choice of the meteorological data used. Heath and Fuelberg (2014) focused on simulated high-resolution data to investigate the impact of rapid vertical transport to the AMA. Both of these studies highlighted the importance of the Tibetan Plateau with respect to transport from the PBL to the AMA. During the monsoon season 2017 comprehensive flight measurements have been conducted in the core of the AMA within the StratoClim campaign (Bucci et al., 2020). Related to the flight campaign, two trajectory studies assessed the transport mechanisms and source regions of the air masses within the AMA in 2017: Bucci et al. (2020) analyzed the PBL source regions of air masses along the flight tracks to determine the source regions of the in-situ sampled air masses.

Legras and Bucci (2020) studied the transport properties to and within the AMA and came to the conclusion that the conduit is

60 driven by convection, whereas further ascent ~~is driven by~~ follows the large scale anticyclonic circulation. This finding is also in agreement with the upward circling in the UTLS, which follows the first rapid ascent in the AMA region, as diagnosed by Vogel et al. (2019).

Despite these previous efforts, there is still a lack regarding the climatological picture and the description of the interannual and subseasonal variability of PBL to AMA transport. The typical short term or single season analysis presented in previous

65 studies need to be tested for robustness, in particular if one considers the strong interannual and intraseasonal variability of the AMA (e.g. Randel and Park, 2006; Garny and Randel, 2013; Siu and Bowman, 2020, and references therein) and of the whole monsoon system (e.g. Krishnamurti and Bhalme, 1976; Ding, 2007).

There are previous modelling studies, e.g. by Chen et al. (2012) and Fan et al. (2017), that looked into a multiannual analysis in the ASM region. However, these studies did not explicitly focus on transport from the PBL to the AMA but rather to a broad

70 ASM region in the UT. As observations (apart from otherwise limited satellite data) are still rather scarce in the AMA region (Brunamonti et al., 2018) and cannot directly provide information on the source region contributions, modelling studies are key to provide a climatological perspective of PBL to AMA transport without temporal or spatial gaps.

One example of the interannual variability of the AMA is the interannual variation of the east–west displacement of the center of the AMA (Wei et al., 2014). Wei et al. (2014) found a relation of enhanced Indian summer monsoon precipitation to

75 the westward displacement of the AMA, which is supported by their simplified modelling studies (see also Wei et al., 2015, for further analyses on the interannual variability of the AMA). Anomalous vertical wind fields in the UTLS over the ASM region corresponding to the longitudinal location of the AMA were shown by Nützel et al. (2016, their Fig. 14). This finding points toward a possible relation of the east–west displacement of the AMA with the transport characteristics in the ASM.

With respect to the intraseasonal variability, Vogel et al. (2015) found a strong variability in the source region contributions

80 to the AMA at 380 K during the monsoon season 2012. This result highlights the need to assess the evolution of the source regions of the AMA air masses during the course of the monsoon season in more detail.

With this additional viewpoint, we aim to bring together results of previous analyses and to add to the understanding of the composition of the AMA. The key questions we want to address are:

1. What is the climatological perspective of PBL to AMA transport in terms of pathways and PBL source regions? How

85 reliable are previous results?

2. How do the pathways and source regions vary on intraseasonal and interannual time scales?

3. Are the PBL source regions and the transport pathways related to interannual east-west shifts of the AMA?

Our main focus lies on the analysis of backward-trajectories, which start in the core of the AMA, are driven by reanalysis data and are followed backward in time to their ~~PBL origin.~~ first crossing of the top of the PBL (Sect. 3). Further, the results

90 from the trajectory analyses will be discussed with additional analyses from chemistry-climate model (CCM) simulations with a Lagrangian transport model ~~.~~ (Sect. 4). In particular, the Lagrangian CCM results are from a free-running simulation and

include the impact of parametrized Lagrangian convection. Results from ~~this~~ the Lagrangian model will serve as a sensitivity in comparison to the reanalysis-based backward trajectory results as (i) (parametrized Lagrangian) convection, (ii) a different large scale dynamical background and (iii) forward trajectories (analyzed backward in time) are considered. This will help us to carve out key features that are similar or sensitive to the different modelling approaches. Further, the multiannual Lagrangian CCM data allow for additional analyses to complement the findings in the trajectory model data.

~~The remainder of this study is structured as follows: Section 2 describes the data and methods used, including short descriptions of the employed models. The section thereafter (Sect. 3) contains the results of the trajectory simulations. These are complemented by the results of the Lagrangian CCM simulations in Sect. 4 and discussed in Sect. 5. Finally, we summarize our findings and state our concluding remarks (Sect. 6).~~

2 Data and method

2.1 Trajectory model data

In this study, we mainly focus on the analysis of data from a trajectory model to investigate the transport from the top of the PBL to the AMA. The trajectory model, which was used to calculate the backward trajectories starting in the monsoon region, was described by Garny and Randel (2016). This trajectory model propagates a set of trajectories, which are initialized by the user, using meteorological data e.g. from reanalysis data sets. ~~Details on the trajectory model setup will be described in the next subsection and the reanalysis data is described at the end of this section.~~

~~Further, data from a CCM including a Lagrangian transport model (Brinkop and Jöckel, 2019), which features a Lagrangian convection parametrization, will be employed to complement the trajectory model results. This modelling approach differs from the trajectory model, e.g. as air parcels of the Lagrangian transport model are initialized only once at the start of the simulation. These air parcels persist and can be followed throughout the simulation. During the runtime of the host-model (Eulerian grid point CCM), the Lagrangian transport model performs online calculations to advance these air parcels using the host model's dynamics. The model output is then used to track back air parcels from the AMA to the PBL. A brief description of the CCM with Lagrangian transport will be presented after the description of the trajectory model.~~

2.2 ~~Trajectory model data~~

~~The trajectory model, which was used to calculate the backward trajectories starting in the monsoon region, was described by Garny and Randel (2016).~~ As for the kinematic calculations presented by Garny and Randel (2016) we have used a time step of 0.5 h and input data from six-hourly ERA-Interim data (Dee et al., 2011) with a horizontal grid spacing of $1.5° × 1.5°$ on 37 pressure levels from 1000 hPa (surface) to 1 hPa to calculate the trajectories.

For ~~our trajectory calculations each day during Northern Hemisphere (NH) summer (01 June to 31 August)~~ each day of the trajectory calculations a set of trajectories with one degree horizontal grid spacing in the region 10-50° N × 0-150° E at 150 hPa was initialized at 00 UTC ~~. This period covers the late ramp-up and the mature phase of the AMA (Mason and Anderson, 1963).~~

~~The trajectories were calculated backward up to~~ and calculated backwards for 90 ~~days.~~ days. Output (e.g. trajectory position and sur-face pressure below the trajectory) was produced every six hours and all analyses for the trajectory model data described here

125 were performed offline on the output data. In ~~total 14 summer monsoon seasons in the period 1979-2013 have been selected~~ ~~as they showed a rather eastward or westward displacement of the AMA. Therefore, a modified version of the so-called South~~ ~~Asian High Index (SAHI; Wei et al., 2014), which measures the longitudinal displacement of the AMA, has been employed. A~~ ~~detailed explanation for the choice of the years and a description of the selection process is given in Sect. 2.3 and the Appendix~~ ~~A2. In the~~ the following, results from the trajectory model will be also indicated via the abbreviation TRJ (short for TRaJectory).

130

We note here that there is a variety of approaches to calculate trajectories from or to the upper troposphere in the AMA region. For example, Bergman et al. (2013) mainly focused on kinematic trajectories to investigate PBL to AMA transport. Similarly, Fan et al. (2017) used kinematic trajectories to calculate the transport from the PBL to the UT in the AMA region. Other studies employed kinematic and/or diabatic trajectories in combination with observed cloud top heights to investigate

135 transport processes in the ASM region (e.g. Bucci et al., 2020; Legras and Bucci, 2020) or hybrid diabatic trajectories (e.g. Vogel et al., 2015, 2019). Based on Lagrangian transport model data from the CCM, we will also address the influence of ~~(hybrid) diabatic versus (hybrid)~~ diabatic versus kinematic trajectories.

2.2 EMAC-ATTILA data

In this study, we also exploit Lagrangian model data from ~~a CCM simulation~~ two CCM simulations described by Brinkop and

140 Jöckel (2019)~~. In this simulation~~, which incorporate the effect of parametrized Lagrangian convection. In these simulations, the CCM EMAC (ECHAM/MESSy Atmospheric Chemistry; Jöckel et al., 2016), was run together with the most recent ver-sion of the submodel ATTILA ~~(Atmospheric Tracer Transport In a LAgrangian model; Reithmeier and Sausen, 2002), which~~ ~~calculates~~ (Atmospheric Tracer Transport In a LAgrangian model; Reithmeier and Sausen, 2002; Brinkop and Jöckel, 2019), which calculated the Lagrangian transport of air parcels ~~(Brinkop and Jöckel, 2019). Within this~~ once with a diabatic and once with

145 a kinematic vertical velocity scheme. For the diabatic scheme the vertical velocity transitions from a mixed kinematic-diabatic velocity to a pure diabatic vertical velocity in the stratosphere (see Brinkop and Jöckel, 2019, and references therein). This mixed coordinate allows to overcome some of the problems associated with pure diabatic trajectories in the troposphere mentioned by Bergman et al. (2013) and by Honomichl and Pan (2020). The corresponding model results of the diabatic and kinematic simulation will be referred to as LG-D and LG-K, respectively.

150 Within these two EMAC-ATTILA ~~simulation~~ simulations - which have the same grid point meteorology - about 1.16 million air parcels, which represent the global atmosphere, are initialized once at the beginning of the simulation and are consequently transported online with a model time step of 600 s according to the CCM's ~~wind~~ meteorological fields (Brinkop and Jöckel, 2019). ~~ATTILA can be operated with diabatic and kinematic transport as provided by the CCM (Brinkop and Jöckel, 2019).~~ ~~Further, since~~ Since its newest update~~ATTILA can~~, ATTILA can also be used with a Lagrangian convection parametrization,

155 which is consistent with the ~~grid-point~~ grid point convection scheme: based on the mass fluxes of the grid point convection scheme - as provided by the host model - air parcels within a column have a probability to be vertically displaced due to

convection such that there is no net vertical air parcel transport between grid boxes, i.e. the number of air parcels in each grid box remains unchanged (Brinkop and Jöckel, 2019, see in particular their Section 2.2.4). ~~The EMAC-ATTILA data used in this study incorporates the effects of parametrized Lagrangian convective transport and either a diabatic or kinematic vertical velocity scheme was employed. In the following, the corresponding model results will be referred to as LG-D and LG-K, respectively.~~

The underlying EMAC ~~simulation has~~ simulations have a grid point spacing of roughly ~2.8° x 2.8° and the model top is located roughly at 0.01 hPa (Brinkop and Jöckel, 2019). The meteorology of the ~~grid-point~~ grid point model evolves freely (Brinkop and Jöckel, 2019), i.e. it is not restrained by observed meteorology, and is hence described as free-running. ~~Here we employ the ten hourly output of the model data~~ The meteorological and Lagrangian data is available only every ten hours, a restriction owing to the large amount of data in the long-term CCM simulations. For further details regarding the simulation ~~setup see the Appendix (Sect. ??) and~~ setups see Brinkop and Jöckel (2019).

2.3 Analysis method

To analyze transport from the top of the PBL to the AMA, we retrace the pathways of individual trajectories or air parcels during NH summer (01 June to 31 August) for both, the trajectory model and EMAC-ATTILA. This period covers the late ramp-up and the mature phase of the AMA (Mason and Anderson, 1963). For both modelling approaches, the trajectories are followed up to 90 days backward in time. When the pressure ~~below the trajectory~~ at the trajectory position is larger than 0.85 times ~~surface pressure~~ the surface pressure below the trajectory, we assume that the trajectory has encountered the PBL as described by Bergman et al. (2013). The first location where this happens backward in time will be referred to as boundary layer source of the trajectory.

Fig. 1 shows the definition of the PBL source regions used in this study: The TP (mainly the Tibetan Plateau) and IP (mainly the so-called Iranian Plateau) regions are defined as regions with a surface elevation of more than 2 km and 0.5 km in the boxes $75\text{--}110°\,E \times 25\text{--}45°\,N$ and $40\text{--}75°\,E \times 25\text{--}40°\,N$, respectively. The other source regions are named AF (mainly parts of Africa and the Arabian Peninsula), WIO (Western Indian Ocean), EIO (Eastern Indian Ocean), IND (mainly the Indian subcontinent), SEA (mainly consisting of Southeast Asia and parts of Southeast China) and the WP (West Pacific) region.

For our analyses the focus will lie on trajectories that start within the AMA, unless otherwise noted. We define the AMA boundary using a geopotential height anomaly (GPHA) criterion with respect to the 50° S-50° N mean as proposed by Barret et al. (2016; see details in the Appendix A1). For the trajectory model data the boundary of the AMA was determined via a ~~geopotential height anomaly (GPHA)~~ GPHA threshold of 280 m using ERA-Interim data (see Appendix A1 for details). Consequently, all trajectories that show a GPHA of at least 280 m are said to be located within the AMA. Sensitivity studies with a GPHA of 260 m for the trajectory model data showed that our qualitative results are not overly sensitive to the choice of the GPHA threshold. For the EMAC-ATTILA analyses (Sect. 4) a separate threshold (of 295 m) for the boundary of the AMA was determined (see Sect. A1). This was necessary as the EMAC-ATTILA simulation is free-running (as noted before) and thus develops slightly different climatological states e.g. with respect to the temperature (Jöckel et al., 2016). As the number

of trajectories that start within the AMA varies from year to year in our analyses, we first calculate the respective distributions before producing the multiannual mean. Hence, each year contributes equally to the presented analyses.
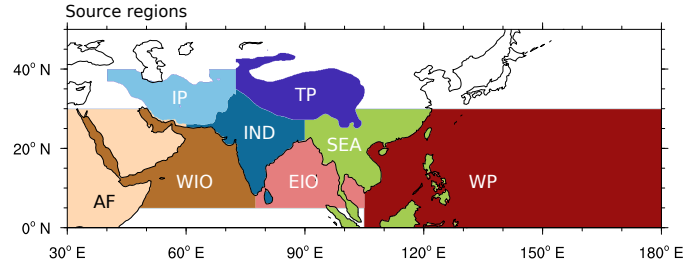
Figure 1. Source regions based on ERA-Interim orography and land-sea mask data at 0.125°x0.125° grid spacing for the TRJ calculations. See text for details.

2.3.1 TRJ

For the trajectory model, the daily initialized (backward) trajectories are followed backwards in time based on the six hourly output of the data. In total, trajectory model data for 14 NH summer seasons (from 01 June to 31 August) out of the period 1979 to 2013 have been analyzed. Choosing these 14 years was motivated by the finding that anomalies of the vertical velocity in the AMA region are related to the position of the AMA (Nützel et al., 2016, their Fig. 14). Hence, we assumed that the transport properties might be related to the mean position of the AMA. Accordingly, the selected 14 summer seasons have been chosen out of the period 1979 to 2013, as the anticyclone showed a rather eastward (seven summer seasons) or westward location (seven summer seasons) during these years. ~~Further details on the selection method are~~ For the selection a modified version of the so-called South Asian High Index (SAHI; Wei et al., 2014), which measures the east–west displacement of the AMA, has been employed. The modification, which uses the geopotential height at three pressure levels - compared to one as originally defined by Wei et al. (2014) - is supposed to better capture the 3D structure of the AMA. A detailed explanation for the choice of the years and a description of the selection process is given in the Appendix A2.

In Fig. 2 we show the differences of vertical velocities at 150 hPa for the two composites (west minus east). Stronger upward motion over the Indian subcontinent and the Tibetan Plateau (TP) is found for the west composite compared to east composite, whereas the years with an eastward shifted AMA show stronger upward motion to the east. Here, we note that we will focus on the joint analyses of all 14 NH summer seasons for the majority of our analyses and address differences between east and west years with additional dedicated analyses.

2.3.2 EMAC-ATTILA

For the EMAC-ATTILA simulation we use each of the ten hourly output time steps of the model data and perform our analyses for 30 NH summer seasons (again, 01 June – 31 August) from 1981 to 2010. Due to a processing error for the LG-K data the year 2008 had to be removed. ~~As already described before,~~ The trajectories in EMAC-ATTILA ~~the trajectories~~ persist through-
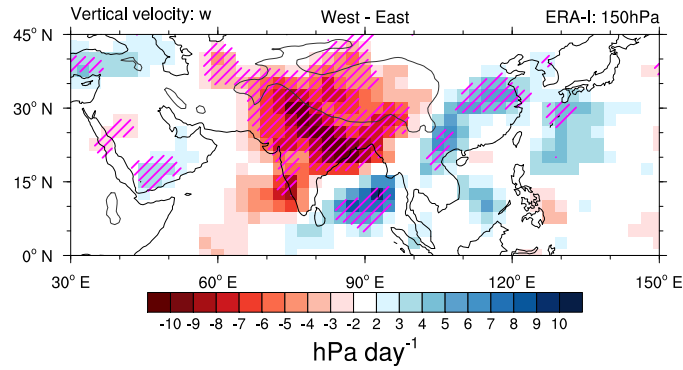
Figure 2. Composite difference of ERA-Interim vertical velocities (in hPa day^{-1}) at 150 hPa (west minus east). Magenta hatching indicates the significance level of 10%. ~~The outlines~~ Black contours show the 2 km outline of ERA-Interim orography to highlight the TP~~are given as black contours based on ERA-Interim data~~. The vertical wind fields were horizontally smoothed prior to the analysis.

out the ~~full simulation period, hence, the individual air parcels are~~ simulation and are thus distributed freely. ~~Thus, we perform our analyses at each output time step (every ten hours) for all parcels that are located inside the AMA ,~~ Hence, they are hardly

215 ever located at (numerically) exactly 150 hPa and we have to use a pressure range (140–160 hPa) instead of a single pressure level (150 hPa for TRJ) to trace back air parcels from the AMA (i.e. parcels that satisfy the geopotential height anomaly criterion and are located ~~on~~ in the NH within 60° W-180° E~~, within the pressure range of 140–160 hPa~~) to their PBL origin. As mentioned before, for the free-running EMAC-ATTILA simulation a different geopotential height anomaly threshold for the definition of the AMA needed to be derived than for the TRJ data (see Sect. A1).

220 Further, all analyses were conducted based on the underlying EMAC model grid. In particular, for the analysis of EMAC-ATTILA data the respective boundary layer source regions (cf. Fig. 1) were defined based on the underlying horizontal resolution of the base model.

2.4 Reanalysis data

ERA-Interim data (Dee et al., 2011; European Centre for Medium-Range Weather Forecast (ECMWF), 2011) at $1.5° \times 1.5°$

225 horizontal grid spacing are used to calculate the TRJ data. Additionally, ERA-Interim data (partly also at different resolutions) are employed for the interpretation of the TRJ data (e.g. to provide corresponding meteorological fields, land–sea masks, orography etc.) and in complementing analyses.

3 Trajectory model results

As already stated, we will focus on the analysis of the trajectory model results (TRJ). Figure 3 shows the starting probabilities of trajectories located within the AMA, i.e. the fraction of days during JJA for which the starting positions of the trajectories are located within the AMA at 150 hPa at a certain grid point for the trajectory model calculations. The corresponding starting probabilities for years with a rather eastward or westward displacement of the AMA (see Appendix A2) are given as cyan solid and ~~purple~~ magenta dashed contours, respectively.
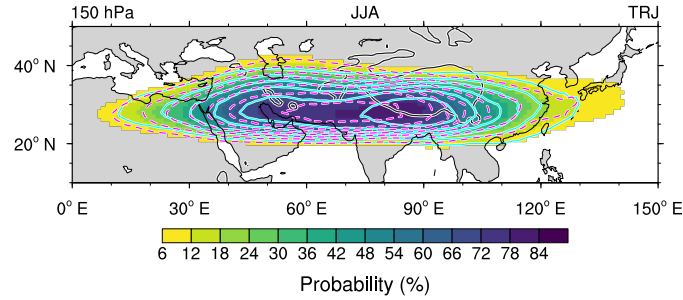
Figure 3. Probabilities (%) of starting locations for trajectories that start within the AMA at 150 hPa during JJA in the TRJ calculations. Trajectories have been started at each $1°x1°$ point per day within the region 10-50° N × 0-150° E and are said to be located within the AMA if the geopotential height anomaly from ERA-Interim (at 1.5° grid spacing) was higher than 280 m (see text for further details). ~~Black~~ Again black contours show the ~~3~~2 km outline of ERA-Interim orography~~, highlighting the TP~~. ~~Purple~~ Magenta dashed (cyan solid) contours (starting at 12% in steps of 12%) show the starting probabilities for the west (east) composites (see Sect. 2.3 for details).

3.1 Climatology and interannual variability

First, we will start investigating the climatological properties of the transport pathways and the PBL sources of air masses from the AMA in the TRJ data with additional notes on the interannual variability. The intraseasonal variability will be discussed thereafter.

3.1.1 Transport pathways

Figure 4 shows the probability density of crossing locations of trajectories for specific height levels, i.e. 200 hPa, 300 hPa, 400 hPa and the boundary layer (defined as 0.85 times surface pressure) in the TRJ calculations. This analysis is analogous to the analysis shown e.g. in Fig. 4 of Bergman et al. (2013). In all panels only trajectories that reach the PBL within 90 days of their release are accounted for. Our results show that during JJA on a climatological basis, AMA air mass sources come from a broad region in the PBL in Asia (bottom right panel) and with increasing height, the upward transport of air masses focuses on the eastern side of (or below) the AMA. Thus, our multiannual trajectory analyses support the findings for August 2011 presented by Bergman et al. (2013) with respect to the final crossing points of ~~PBL to AMA trajectories~~ the PBL of trajectories that ascend to the AMA.
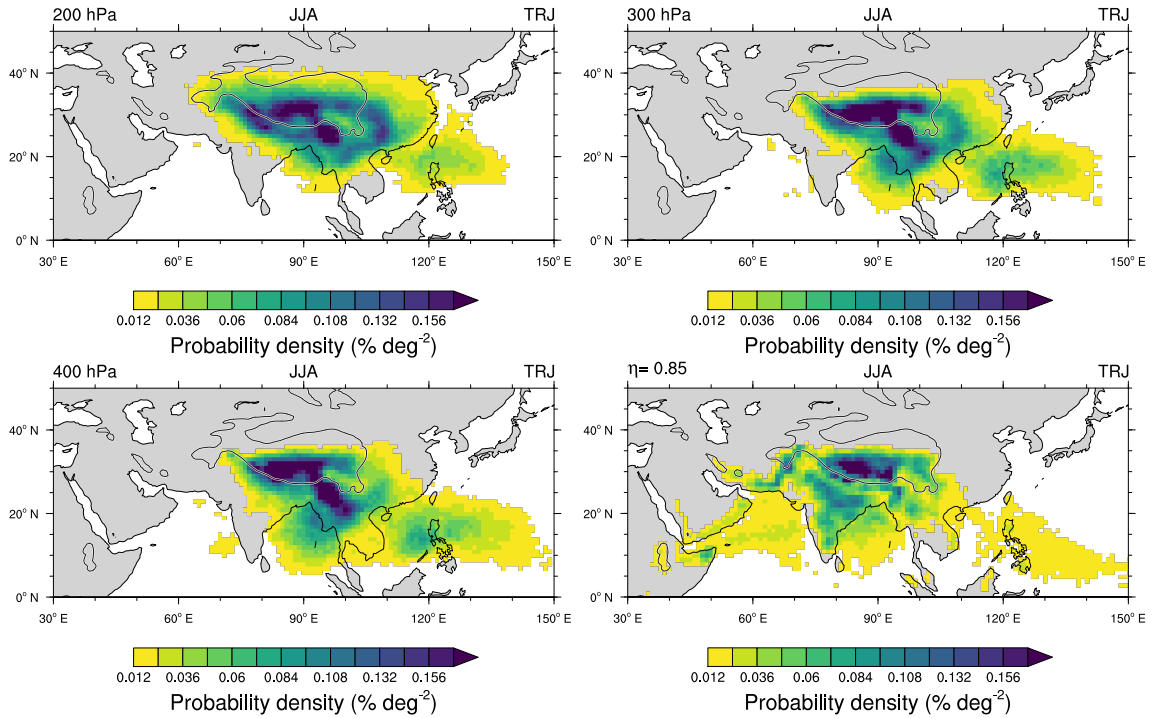
Figure 4. Probability density (% deg^{-2}) of trajectory (upward) crossings at (top left) 200 hPa, (top right) 300 hPa, (bottom left) 400 hPa and (bottom right) the PBL (defined as 0.85 times surface pressure) for trajectories that start within the AMA and cross the PBL (as defined before). As noted before, for the 14 years the individual distributions have been calculated and averaged afterwards, i.e. each year contributes equally to the probability density (also for subsequent analyses). Here and in the following plots, if the last bin of the colour bar is denoted by a triangle, it contains all values up to the maximum of the field, which is plotted.

However, we point out that by construction this analysis only captures the regions of upward transport to the AMA and not necessarily the full three-dimensional pathways. To highlight this difference, Fig. 5a shows the density of trajectories that

250   have fallen below 200 hPa and have risen again above 195 hPa (backward in time). This analysis points out the locations of downward transport ~~. Approximately~~ and approximately half of all PBL crossing trajectories experience this ~~re-circulation at this pressure level in the depicted region~~downward motion at the depicted level.

To simplify the interpretation a clarifying schematic for two hypothetical PBL-crossing trajectories (trj1 and trj2) is shown in Fig. 5~~(right panel)~~b: The positions of trj1 and trj2 at the red dots would be noted in Fig. 4 - showing regions of upward

255   transport, i.e. the final crossing points of a certain level of the trajectories. Whereas the position of trj1 at the blue dot would be noted in Fig. 5b - highlighting regions of downward transport.

~~Thus, the emerging picture is in agreement with upward circling, which follows the first updraft as described by Vogel et al. (2019) and Legras and Bucci (2020). The transport pathways further fit with the distribution of mean vertical velocities in the UTLS in the~~
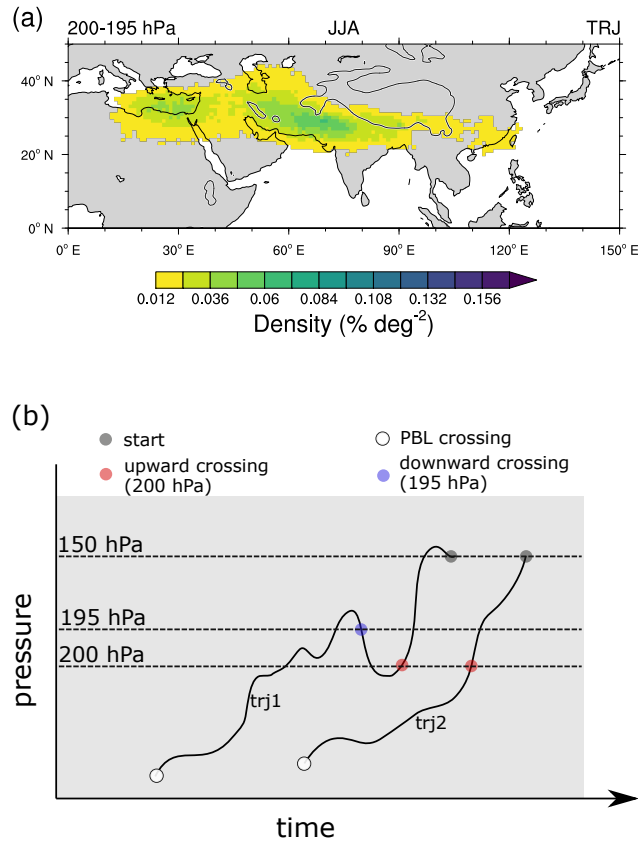
Figure 5. ~~(Left)~~ **(a)** Density (% deg^{-2}) of trajectory (downward) crossings at 195 hPa for trajectories that start within the AMA and cross the PBL (as defined before) and fall below 200 hPa before they reach the final destination at 150 hPa. ~~(Right)~~ **(b)** Schematic of trajectory crossings described in the left panel of this figure and in Fig. 4. See text for details.

~~monsoon region (e.g. Nützel et al., 2016, their Fig. 10) as well as tracer transport and distribution as discussed by Pan et al. (2016;~~

260 ~~cf. also their discussion on the large scale circulation in the AMA region).~~

To get a better picture of the full transport pathways, we show the distributions of PBL crossing trajectories as a longitude vs. log-pressure height cross section in Fig. 6. The scale height was chosen as 7 km as was done e.g. by ~~Abalos et al. (2017)~~ Abalos et al. (2017; see also for log-pressure height formula) and the reference pressure of 1013.25 hPa as in the base model of the EMAC-ATTILA simulations (cf. Roeckner et al., 2003, for details on ECHAM5). The individual panels show the temporal evolution of the tra-

265 jectories that start within the AMA, 1 day, 2.5 days, 5 days and 15 days prior to their release (top left to bottom right panel, respectively). For orientation purposes meteorological data from ERA-Interim is overlaid (see Fig. caption for details).

Obviously, as noted by Bergman et al. (2013) the main upward transport occurs on the eastern side below the anticyclone (centered around $\sim$90° E), however, as already indicated above, the trajectories start to fill the AMA well below the initial

270 release height (150 hPa) ~~. Again this points towards an upward circling already considerably below 150 hPa for some of the trajectories and refines the original conduit schematic as depicted and discussed by Bergman et al. (2013). As pointed out before, this is also in accordance with the large scale uplift above 360 K described by Vogel et al. (2019) in particular, if one considers that the release height of our trajectories is mostly above 360 K (see cyan lines in~~ and downward transport occurs on the western side of the AMA (Fig. ~~6~~5a). It is worth noting that 15 days prior to release a considerable fraction of trajectories

275 has reached the PBL above the TP (maximum in the density around 5 km and 70-100° E in Fig. 6 lower right panel).

The complementing latitude versus log-pressure height cross section of the climatological trajectory positions for JJA is shown in Fig. 7. Here, the trajectory positions (left) 5 and (right) 15 days prior to their arrival at 150 hPa are depicted. Again, meteorological data from ERA-Interim is overlaid to facilitate the interpretation. The trajectory distribution around the AMA

280 height levels is tilted from North to South, in agreement with a tilt of the isentropic levels (see cyan lines in Fig. 7). We note that the distribution shows high values above or around the slopes of the Himalayan mountains (roughly at 30° N) and that over time more and more trajectories reach their PBL source region over the TP (max. around 5 km and 30-35° N) and to its south.

From the presented analyses, the emerging picture of PBL to AMA transport is in agreement with upward circling, which

285 follows the first updraft as described by Vogel et al. (2019) and Legras and Bucci (2020). This upward circling srefines the original conduit schematic as depicted and discussed by Bergman et al. (2013). The transport pathways further fit with the distribution of mean vertical velocities in the UTLS in the monsoon region (e.g. Nützel et al., 2016, their Fig. 10) as well as tracer transport and distribution in a CCM as discussed by Pan et al. (2016; cf. also their discussion on the large scale circulation in the AMA region). Additionally, CO distributions from chemistry transport model data presented by Barret et al. (2016) support

290 this view on PBL to AMA transport, while in their climatological analysis of IASI satellite data the structure was not as conclusive. Using data from the same satellite instrument, but performing transient analyses, Luo et al. (2018) came to the conclusion that this transport behaviour is also present in the satellite data. Similarly, Vogel et al. (2019) noted that the CO transport described by Pan et al. (2016) is in agreement with their results from a trajectory model and MIPAS satellite data. We stress here, that the trace gas based results (e.g. in modelling or satellite data) strongly depend also on the strength and location

295 of emissions, whereas the idealized trajectory studies simply track air mass transport.

We will now address the sensitivity of the presented results with respect to east-west shifts of the AMA on interannual time scales. Therefore, Fig. 8 shows the differences in the upward transport regions for west minus east years. Differences are clear in the upper level (200 hPa) and fit to the differences in the vertical wind fields in the UT (cf. 150 hPa level in Fig. 2). The

300 differences are less pronounced at the top of the PBL (defined as 0.85 times surface pressure).

To capture the differences in the full pathways, Fig. 9 shows the differences of the density distributions of the trajectories (west minus east years) as longitude vs. pressure cross section on individual dates with respect to the initialization date. Whereas differences are pronounced and significant shortly after the release of the trajectories in the UT, they get less pronounced and

clearly less significant at lower levels. Overall, we note that the qualitative results regarding the transport pathways remain stable.

3.1.2 Boundary layer source regions

In the following, we want to further analyze from which PBL source regions (see Fig. 1) air masses within the AMA originate. ~~Therefore, Fig. 1 shows the definition of the individual source regions. The TP (mainly the Tibetan Plateau) and IP (mainly the so-called Iranian Plateau) regions are defined as regions with a surface elevation of more than 2 km and 0.5 km in the boxes 75–110° E × 25–45° N and 40–75° E × 25–40° N, respectively. The other source regions are named AF (mainly parts of Africa and the Arabian Peninsula), WIO (Western Indian Ocean), EIO (Eastern Indian Ocean), IND (mainly the Indian subcontinent), SEA (mainly consisting of Southeast Asia and parts of Southeast China) and the WP (West Pacific) region.~~

~~Contributions from different source regions to AMA air masses at 150 hPa during JJA. The categories resX and noX correspond to the trajectories that reached the PBL outside the defined source regions (see Fig. 1) or did not reach the PBL within 90 days prior to their start, respectively. TOT corresponds to the total numbers of trajectories released within the AMA, where 1 percent corresponds to 4000 trajectories. The mean values are given by blue dots (with blue whiskers for the interannual standard deviation), whereas individual years are shown as grey dots.~~

~~The mean contribution~~ The mean contributions of individual source regions (blue dots) in the TRJ simulation and their interannual ~~variation~~ variations (translucent grey dots and blue whiskers) are shown in Fig. 10. The largest contributions from the named source regions are found from the TP region (around 17%), the IND region (around 13%) and the WP region (around 12%). However, we note that the densities of PBL crossings are larger for the TP and IND region than for the WP region (see Fig. 4). There is also a considerable fraction of trajectories of around 16% that encounter the PBL outside the named source regions (resX) or do not encounter the PBL within 90 days prior to release (noX).

There is strong interannual variability regarding the sources of the AMA as indicated by relatively large whiskers and a considerable spread of the contributions in individual monsoon seasons. Nevertheless, the aforementioned regions, namely TP, IND and WP, are more important for the AMA composition in the TRJ simulation in almost all years than the other source regions. The intraseasonal variability of these source regions will be discussed along with the variability of the transport pathways in the next section (Sect. 3.2).

~~Contributions of PBL air masses to the AMA at 150 hPa split according to the east (cyan) and west (purple) location of the AMA with individual years given as grey dots. The cyan and purple whiskers mark the interannual standard deviation for the east and west composite, respectively. For TOT the total number of trajectories located within the AMA are reported, where 1 % corresponds to 4000 trajectories.~~

~~Figure~~Fig. ~~??,~~ 10 also shows the contributions of different source regions to the AMA split according to the rather eastward (cyan) or westward (~~purple~~magenta) location of the AMA. This analysis shows that there are no systematic differences in the mean source region contributions according to the east–west location of the AMA on interannual timescales and in particular the large interannual variability renders the slight differences between the two composites insignificant. This is in agreement with the previous statement that the main transport pathways did not change qualitatively with respect to the east–

west displacement of the AMA on an interannual basis and that the boundary layer source changes are relatively small or partly compensating within the different source regions as for instance for the TP region (see Fig. 8). With respect to the interannual variability within the composites, the TP region and the total number of trajectories (TOT) show enhanced variability in the east composite whereas reduced variability is found for the IP contribution. Whether this result is robust or not, is unclear. Slightly more trajectories are located within the AMA for years in which the AMA is displaced to the west (in agreement with the higher maximum in the contour lines for westward location of the AMA in Fig. 3). This difference, however, is not significant as there is strong interannual variability as indicated from the interannual standard deviation (included as whiskers in Fig. ??10).

3.2 Intraseasonal variability

3.2.1 Transport pathways

To further analyze the subseasonal variability with respect to the PBL source regions and the transport pathways, Fig. 11 (analogous to Fig. 4) shows maps of final boundary layer and pressure level crossings split according to June, July and August, respectively. As can be seen from these plots the PBL crossings shift over continental Asia over the course of the monsoon season from June to August. Furthermore, the regions of upward transport, which are mainly centered over the eastern Indian Ocean (Bay of Bengal) and adjacent continental regions at 200 and 400 hPa in June, shift northwards towards the TP in July and August.

A more quantitative view of this northward shift is presented in Fig. 12, which show shows the distributions of the latitudinal position of PBL crossings for June (blue), July (red) and August (purple) of trajectories starting in the AMA. In particular, the modal value in June at 5° N is clearly reduced in July (and August) and the contributions around 30° N roughly double from June to July. The interannual variability depicted as dashed lines in Fig. 12, allows to draw the conclusion that this is a typical behaviour throughout the monsoon season.

For a complementing view of the transport pathways during June to August, Fig. 13 shows the distributions of the trajectories in a latitude versus log-pressure height cross section 5 and 15 days before the trajectories encounter their starting position at 150 hPa. It is shown that the trajectory locations shift from south to north during the evolution of the ASM from June to August. In August ,the AMA is located above the TP and transport from the TP into the AMA occurs vertically. We emphasize the clear shift of the maximum density at about 6 km to 10 km from approximately 20° N in June to 30° N in August.

This northward shift of the PBL source regions and the transport pathways is consistent with the northward shift of the region of low outgoing longwave radiation and the AMA (Nützel et al., 2016, their Fig. 12; see also the related discussion) and the monsoon (precipitation) itself (e.g. Wang and LinHo, 2002; Yihui and Chan, 2005). This northward propagation can also be seen in deep convective activity as monitored by satellite measurements, where deep convection (up to 150 hPa) over the TP is rare in June and becomes more prominent in July and August (Devasthale and Fueglistaler, 2010).

3.2.2 Boundary layer sources

Besides the strong interannual variability the AMA is also known for its intraseasonal/subseasonal variability (see e.g. Fig. 5 in Garny and Randel, 2013, showing both interannual and intraseasonal variability). Hence, we now concentrate on the contribution of individual PBL source regions to the AMA air masses with particular focus on the subseasonal variability. Fig. 14a shows the temporal evolution of the source region contributions in the TRJ simulation. The most prominent change is the increase of the TP contribution from below 4% in early June to more than 24% for most of August. Also, it is obvious that the fraction of non-crossing (noX) trajectories clearly decreases over time. This implies that over the monsoon season the fraction of air masses within the AMA that have recently (within the last 90 days) come from the PBL increases. Further, over the course of the monsoon season, the contributions of trajectories that cross the PBL outside the monsoon region (resX) declines noticeably. This indicates that the PBL sources focus more toward the Asian monsoon region and is in accordance with the impression from Fig. 11. The WP region shows a minimum contribution at the beginning of July (below 10%) whereas the contributions in early June (around 16%) and end of August (around 20%) are clearly higher. For the IND region, the evolution is reversed with a peak contribution in July (∼16%) and lower contributions in early June and end of August (about 8% and 12%, respectively). Apart from a small dip in early June, the contribution of the SEA region increases steadily from around 5% in mid June to approximately 9% end of August. For the AF region this behaviour seems to be reversed (from around 5% to 3%). All other source regions (WIO, EIO and IP) show some variation in June but have relatively stable contributions (between about 4-6%) during July and August.

~~Contributions of PBL sources to the AMA at 150 hPa for the TRJ simulation over 14 years split according to June (blue), July (red) and August (purple). The interannual standard deviation is given as whiskers and the individual years are included as grey dots. For TOT 1% corresponds to 2000 trajectories.~~

~~Figure~~

Fig. ~~?? shows the PBL~~ 14b shows the source region contributions split according to June, July and August ~~for the multiannual mean (coloured dots) and individual years (grey dots). This figure is closely related to the analysis shown in Fig. 14 but additionally captures the interannual variability of the subseasonal development and allows to assess, how robust these subseasonal features are. As an example, the~~. The increase in the contribution of the TP from June to August is ~~clearly visible and the separation of the data points for June and August indicates that this is a typical~~ pronounced and present in every single year. Thus it is a robust feature of the intraseasonal variability of AMA air mass contributions. ~~Indeed, the increase of the contribution of TP air masses to the AMA from June to August is present in every single year.~~ Further, except for one year, the TP is the most important source region for air masses within the AMA in August in our analysis. Also, as the resX contribution significantly declines from June to July/August, it is shown that the PBL source regions focus more on the ASM region~~, which is in accordance with Fig. 11. Further, we also note that more~~. More trajectories are located within the AMA in July than in June and August~~. This~~, which is in agreement with the seasonal cycle of the AMA (e.g. Garny and Randel, 2013; Nützel et al., 2016, Figs. 5 and 12, respectively) as already described by Mason and Anderson (1963). For the other source regions,

the intraseasonal variations are overruled by the strong interannual variability and more years would be needed to carve out robust differences.
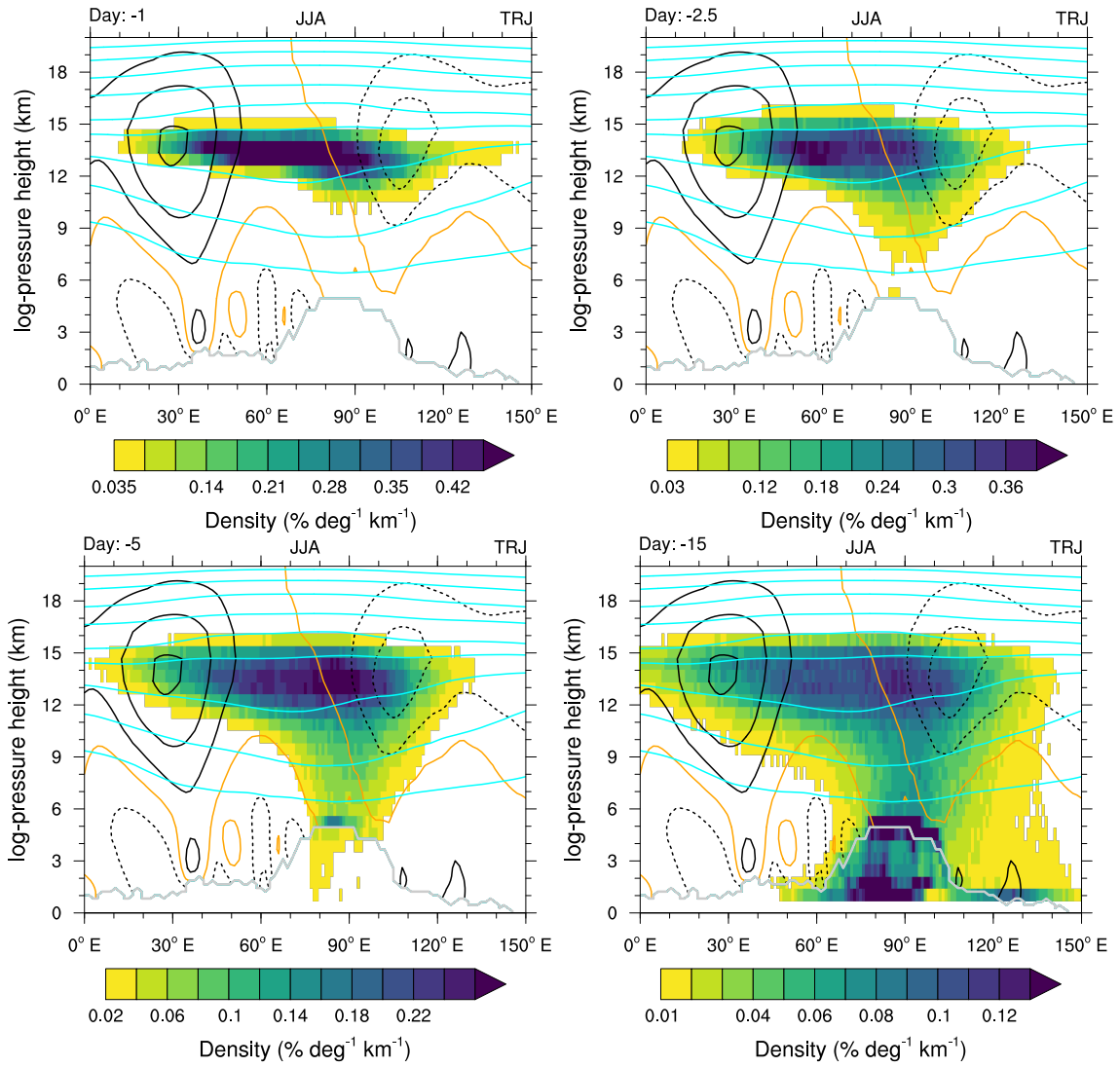
Figure 6. Longitude versus log-pressure height cross sections of density distributions (% deg^{-1} km^{-1}) of trajectory positions for PBL crossing trajectories (top left) 1 day, (top right) 2.5 days, (bottom left) 5 days and (bottom right) 15 days prior to their arrival at 150 hPa within the AMA. The three-dimensional probabilities were integrated over 0-50° N. Please note the different colour bars. The 150 hPa level corresponds roughly to 13.5 km and the 200 hPa level is located at roughly 11.5 km in the plot . For this analysis($p = p_0 e^{-x/H}$, once x in km, H=7 km and $p_0 = 1013.25$ hPa - see text). Once trajectories reach the PBL they their pathways are not followed back any furthertracked and will be . Instead, they are noted at the their first PBL-crossing point points also later for analyses going back further in time. For example, if a trajectory reaches the PBL already after 3 days, it will be counted at this PBL-crossing position also for the analysis 5 days and 15 days back in time. Please note - also for upcoming figures - that the maximum in the distribution at 4-6 km, e.g. present in the bottom right panel, is related to the TP. Cyan lines indicate potential temperature levels at 30° N starting at 340 K to 380 K in steps of 10 K and 20 K afterwards (380 K to 480 K). Black contours indicate meridional winds at 30° N in steps of 3 m s^{-1}. Negative, i.e. southward, winds are dashed and the zero wind line is given in orange. Meteorological data based on ERA-Interim is flagged out below the grey line, which indicates the ERA-Interim minimum surface pressure in the region 0-50° N of the time average JJA for the trajectory years.
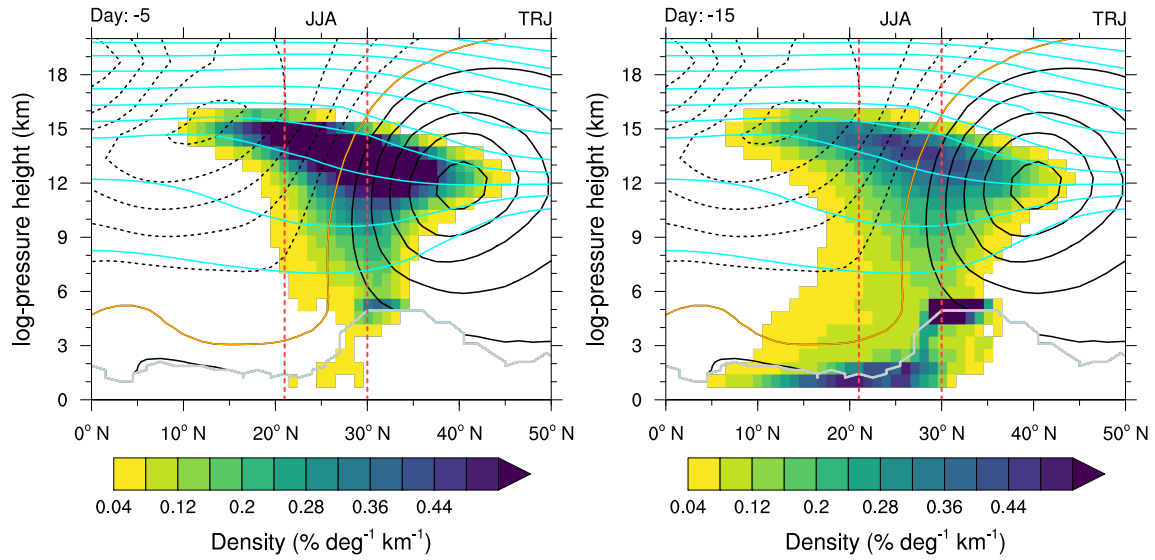
Figure 7. Latitude versus log-pressure height cross sections of density distributions (% deg^{-1} km^{-1}) of trajectory positions for PBL crossing trajectories 5 days and 15 days prior to their arrival at 150 hPa within the AMA. The three-dimensional probabilities were integrated over 60-140° E. The 150 hPa level corresponds roughly to 13.5 km and the 200 hPa level is located at roughly 11.5 km in the plot. ~~For this analysis, once~~ Once trajectories reach the PBL they are not ~~further~~ tracked further and will be noted at the ~~first PBL-crossing~~ crossing point also ~~later further back~~ in time (as in Fig. 6). Cyan lines indicate potential temperature levels averaged over 0-120° E starting at 340 K to 380 K in steps of 10 K and 20 K afterwards (380 to 480 K). Black contours indicate zonal winds averaged over 0-120° E in steps of 5 m s^{-1}. Negative, i.e. westward, winds are dashed and the zero wind line is given in orange. Meteorological data based on ERA-Interim is flagged out below the grey line, which indicates the ERA-Interim minimum surface pressure in the region 0-120° E of the time average JJA for the trajectory years.
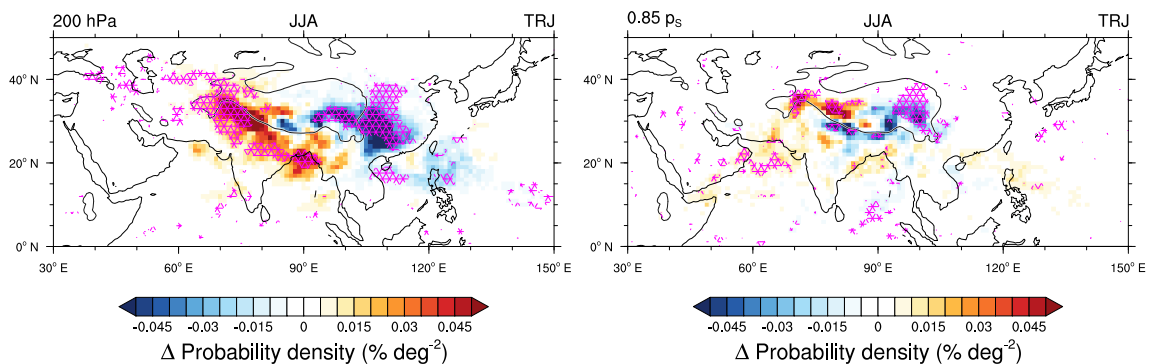
Figure 8. Difference (west minus east years) of probability densities (% deg^{-2}) of trajectory (upward) crossings at 200 hPa and the PBL (defined as 0.85 times surface pressure) for trajectories that start within the AMA and cross the PBL (as defined before). The underlying fields have been horizontally smoothed and the significance level of 0.1 is noted via magenta hatching.
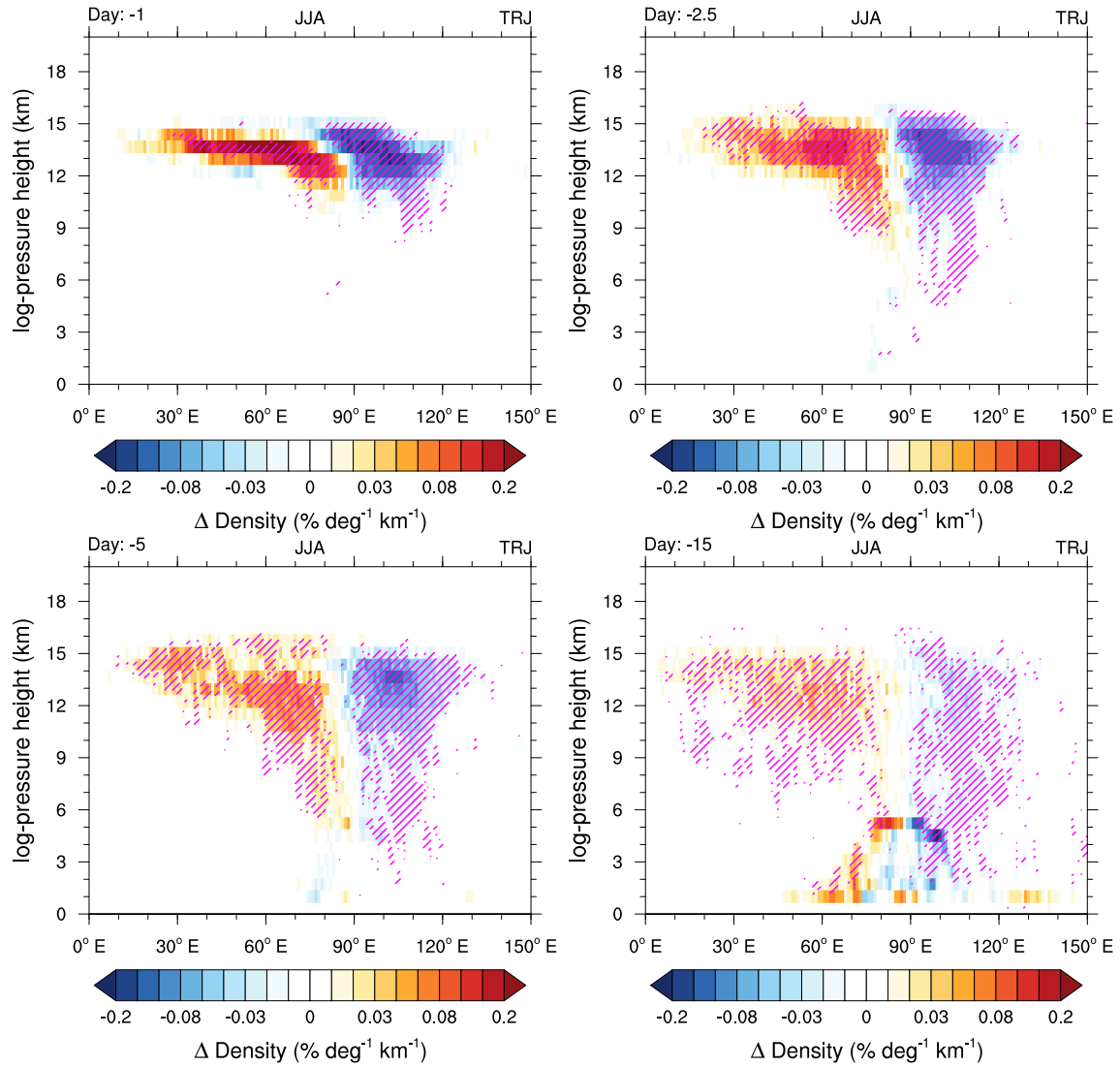
Figure 9. Longitude versus log-pressure height cross sections of the difference (west minus east years) of the density distributions (% deg^{-1} km^{-1}) of trajectory positions for PBL crossing trajectories 1 day, 2.5 days, 5 days and 15 days prior to their arrival at 150 hPa within the AMA. The three-dimensional probabilities were integrated over 0-50° N. The 150 hPa level corresponds roughly to 13.5 km and the 200 hPa level is located at roughly 11.5 km in the plot. Once trajectories reach the PBL they are not ~~tracked~~ further ~~transported~~ and will be noted at the crossing point also ~~later~~ further back in time (as in Fig. 6).
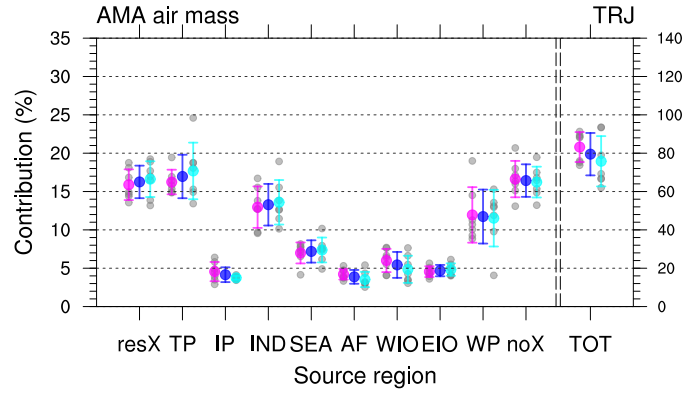
Figure 10. ~~Source~~ Contributions from different source regions ~~based on ERA-Interim orography and land-sea mask data~~ to AMA air masses at ~~0.125°x0.125° grid spacing for~~ 150 hPa during JJA. The categories resX and noX correspond to the ~~TRJ calculations~~ trajectories that reached the PBL outside the defined source regions (see Fig. ~~See text~~ 1) or did not reach the PBL within 90 days prior to their start, respectively. TOT corresponds to the total numbers of trajectories released within the AMA and is given in units of 10^3 trajectories. The mean values are given by blue dots with blue whiskers for ~~details~~ the interannual standard deviation. The mean values and interannual standard deviation split according to the east (west) location of the AMA are given as cyan (magenta) dots and whiskers and the individual years are shown as grey dots.
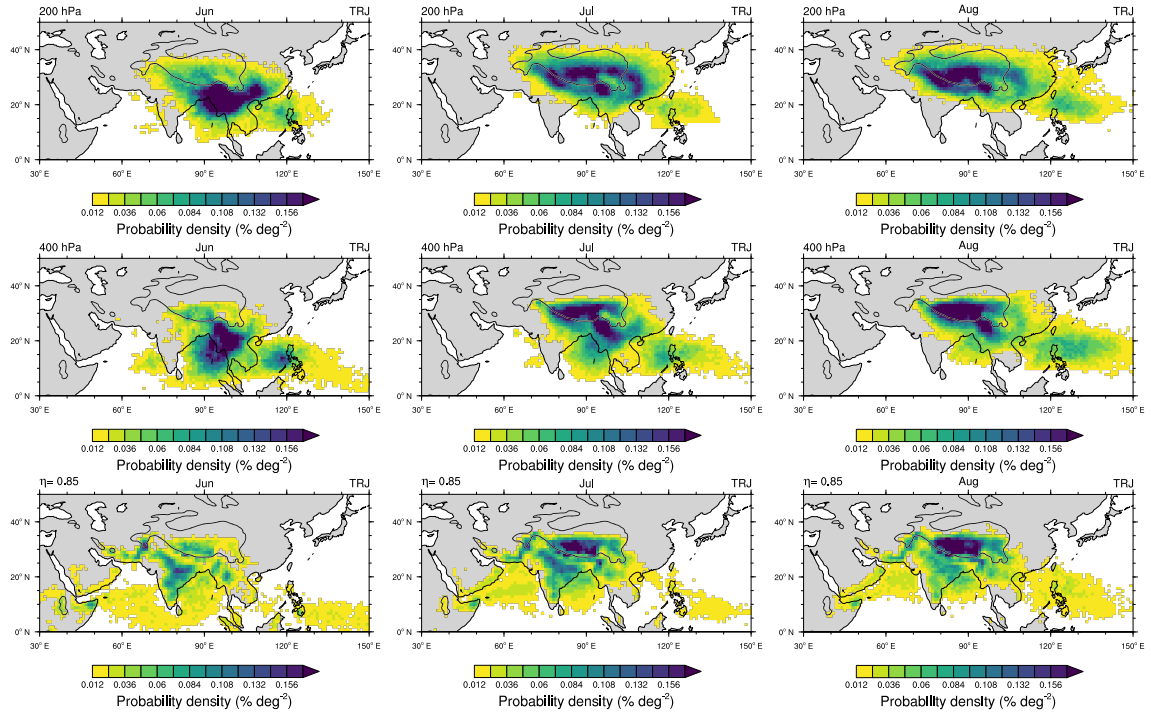
Figure 11. Probability density (% deg^{-2}) of trajectory (upward) crossings at (top row) 200 hPa, (middle row) 400 hPa and (bottom row) the PBL as in Fig. 4 but split according to (left column) June, (middle column) July and (right column) August.
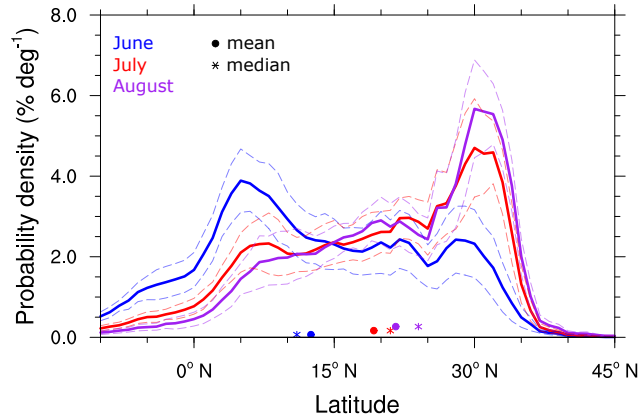
Figure 12. Probability density (% deg^{-1}) with respect to latitude of trajectory intersections with the PBL split according to June (blue), July (red) and August (purple). Mean (dots) and median (crosses) are given as well. Dashed lines mark the interannual standard deviation.
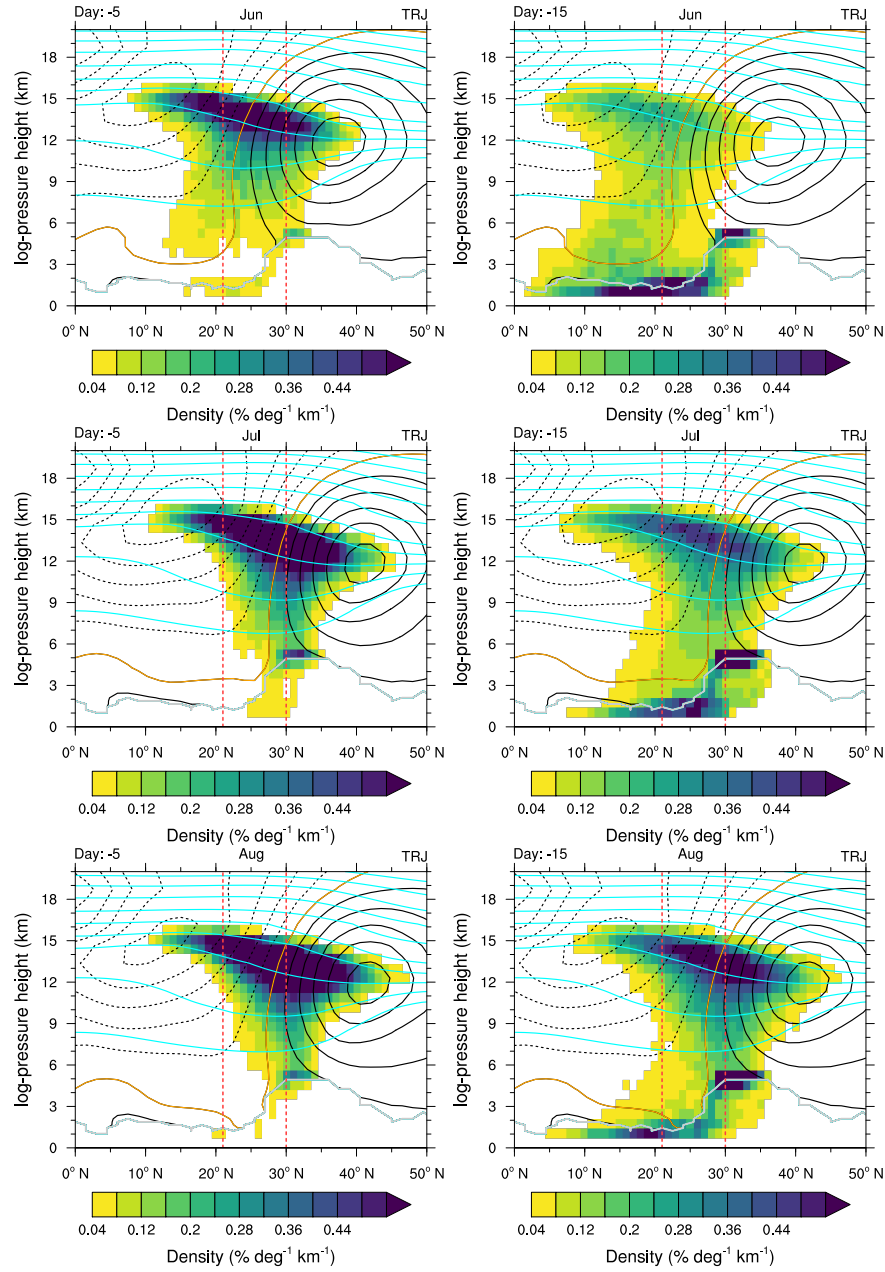
Figure 13. As in Fig. 7 for (left column) 5 and (right column) 15 days prior to their final position at 150 hPa, split according to (top row) June, (middle row) July and (bottom row) August. Again the three-dimensional probabilities were integrated over 60-140° E. For orientation purposes red vertical dashed lines at 21° N and 30° N, roughly indicate the maxima in the distributions between 6 and 12 km for June and August for the trajectories 15 day prior to their arrival at 150 hPa, respectively. Meteorological data from ERA-Interim is presented as in Fig. 7 but separated for June, July and August, respectively.
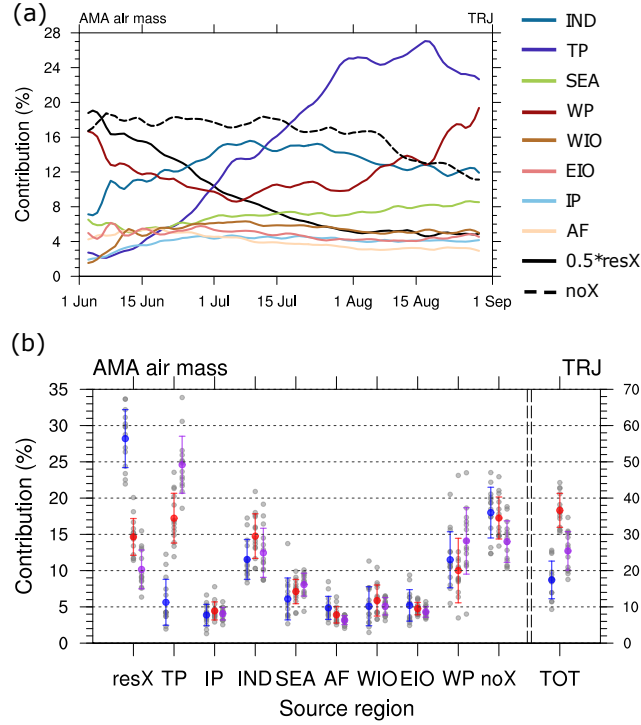
Figure 14. (a) Temporal evolution of source region contribution to the AMA air masses at 150 hPa in the TRJ calculation. To fit the scale the resX category was scaled by 0.5. All contributions have been smoothed via 5 day running means (weights of $[\frac{1}{9}, \frac{2}{9}, \frac{3}{9}, \frac{2}{9}, \frac{1}{9}]$). **(b)** Contributions of PBL sources to the AMA at 150 hPa for the TRJ calculation over 14 years split according to June (blue), July (red) and August (purple). The interannual standard deviation is given as whiskers and the individual years are included as grey dots. For TOT the total number of trajectories is given in units of 10^3 trajectories.

4   EMAC-ATTILA results: a complementary view

To corroborate our results and to point out sensitivities and uncertainties, we show also the results of free-running Lagrangian CCM simulations. As already noted in Sect. 1, the Lagrangian data from these simulations can provide a complementary view because the modelling approach differs largely from the reanalysis driven trajectory data presented in Sect. 3. The EMAC-ATTILA data contain the effect of parametrized convection and stem from two free-running simulations, in which the vertical velocity is described either by a kinematic (LG-K) or a diabatic (LG-D) scheme ~~(cf. Brinkop and Jöckel, 2019).To be precise, the simulations feature a sigma-pressure or sigma-theta vertical coordinate (see Brinkop and Jöckel, 2019). This hybrid coordinate allows to overcome some of the problems associated with diabatic trajectories in the troposphere mentioned by Bergman et al. (2013) and by Honomichl and Pan (2020). For the analyses the forward trajectories of the EMAC-ATTILA data were traced back. Further, all analyses were conducted based on the underlying EMAC model grid. In particular, the respective boundary layer source regions were defined based on the underlying horizontal resolution of the base model.~~ (see Sect. 2).
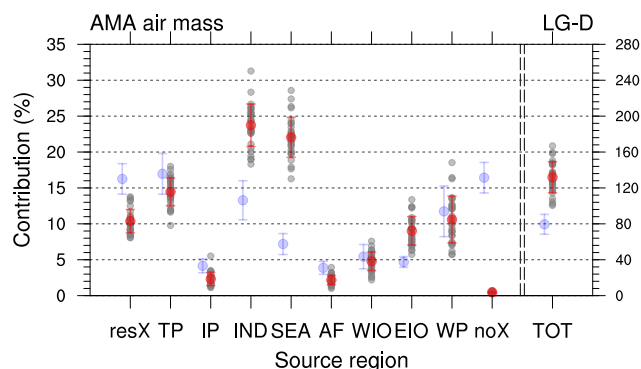
Figure 15. Contributions of PBL sources to the AMA around 150 hPa for 1981-2010 from the free-running LG-D simulation. ~~Whiskers~~ Mean values are given as red dots, red whiskers denote the interannual standard deviation ~~, whereas~~ and individual years are indicated via grey dots. For TOT ~~1% corresponds to 8000~~ the right axis denotes the total number of trajectories in units of 10^3 trajectories. For comparison faint blue dots and whiskers denote the values from the TRJ data.

First, we want to focus on features, where the LG-D simulation support the results of the TRJ calculations. Secondly, we show which results differ and where (a parametrization of) Lagrangian convection might be of importance. Finally, we also address the impact of the vertical velocity scheme by comparing the model results of the LG-D and LG-K.

We have found that the pathways of the LG-D data (see supplemental Fig. B2) look similar to the pathways shown in Fig. 6. Moreover, the LG-D data also show strong interannual variability in the source region contributions (cf. Fig. 15).

Further commonalities in the TRJ and LG-D model data results can be seen, when it comes to the evolution of PBL contributions to the AMA air masses. Both model data show an increase of the TP contribution from June to August (Figs. 14 and
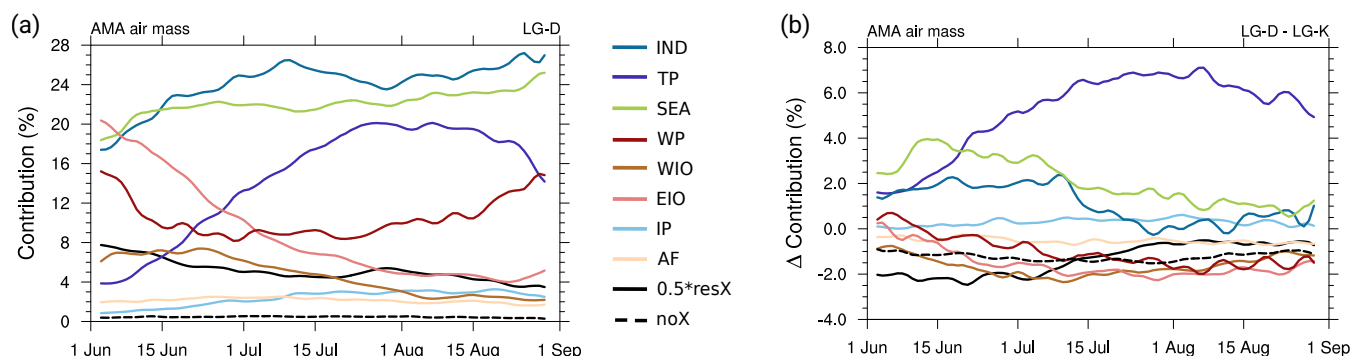
Note: Fig. 16 slightly updated compared to the diff-version in the author comments

Figure 16. ~~Source~~ **(a)** PBL source contribution evolution in the LG-D data. resX data has been scaled by 0.5. All contributions have been temporally smoothed via 5 day running means (weights of $[\frac{1}{9}, \frac{2}{9}, \frac{3}{9}, \frac{2}{9}, \frac{1}{9}]$), while daily data were produced from summing up the ten hourly data for each day. **(b)** as in (a) but for the difference of the source contributions for LG-D minus LG-K. As in the LG-K data the year 2008 is missing (cf. Sect. 2.3), it was also removed in the LG-D data for this analysis. Colour coding as in **(a)**.

16a). Also, the qualitative evolution of the contribution of the WP and SEA regions – minimum contribution during July for
425 WP and slight increase over the monsoon period for SEA – are similar in the two model data sets.

However, we have to note that quantitatively, the contributions differ between the two model data sets (cf. also Fig. 15). As an example the contribution of the TP in August is not as dominant in LG-D as in TRJ. Further, around 11% of the trajectories come from a region outside the defined sources in the LG-D, which is similar to roughly 16% in the TRJ data. However, in the TRJ data this contribution drops considerably from June to August, whereas in the LG-D data the decline is more moderate.
430 The differences between the TRJ and EMAC-ATTILA data are likely to be also related to the faster vertical transport in the LG-D data due to the effect of parametrized convection. As an example, the air masses that do not reach the PBL within 90 days account for more than 15% in the TRJ calculation during JJA, whereas in LG-D this value is below 1%. The differences in this fraction might also be related to the quantitative differences in the contributions of IND and SEA in the TRJ and LG-D data, namely clearly higher contributions in the LG-D data than in the TRJ calculations. An intermediate region is the EIO showing
435 slightly higher contributions in LG-D data, which might hint towards the importance of convective transport from this region, which is located beneath the south-eastern part of the AMA. As the contributions of IP, AF and WIO are relatively small in all model data sets, this indicates that convective transport from these regions to the AMA might not be overly important.

We stress that the above results also hold qualitatively for the LG-K data. Fig. ~~??~~ 16b shows the differences in the contribution of source regions to the AMA air masses for LG-D minus LG-K data. Major differences are that the contribution of the TP is
440 not as large as in the LG-D data and that the increase over the monsoon period is less pronounced (absolute values for LG-K are shown in supplemental Fig. B4). Throughout the monsoon season, the LG-D data show overall higher contributions for TP, IND and SEA compared to the LG-K data. Almost no differences are found for the contribution of the IP, whereas lower contributions are found for the other source regions.

For the LG-D data we analyzed the sensitivity of our results with respect to the method to determine the PBL. We found that
qualitatively the results do not depend on the choice of the PBL criterion, while quantitatively, the changes were in the order of
450 switching between kinematic and diabatic trajectories (i.e. differences in the LG-D and LG-K data) while using the standard
PBL criterion.

As we have found a strong increase of the TP contribution to the AMA air masses over the monsoon season in the TRJ
and LG-D (less so in LG-K) data, we further analyzed for the LG-D data the change of transport properties from the TP to
the UT for June and August. Therefore, Fig. 17 shows the differences (August minus June) in the longitudinal distributions
455 of trajectories that stem from the TP for multiple pressure levels (300-150 hPa in 50 hPa steps). In August compared to June
the trajectories are more likely located in the ASM region (60-100° E), whereas in June the probability is larger east of the
ASM region (and in particular the North American monsoon region sticks out). Further, also the fraction of trajectories from
the TP at the different levels (June with respect to August), decreases with height (from about 90% at 300 hPa to about 70% at
150 hPa), which indicates that transport from the TP to the UT is stronger in August than in June. These results are consistent
460 with stronger advection to the east of air masses from the TP in June compared to August due to the location of the subtropical
jet.
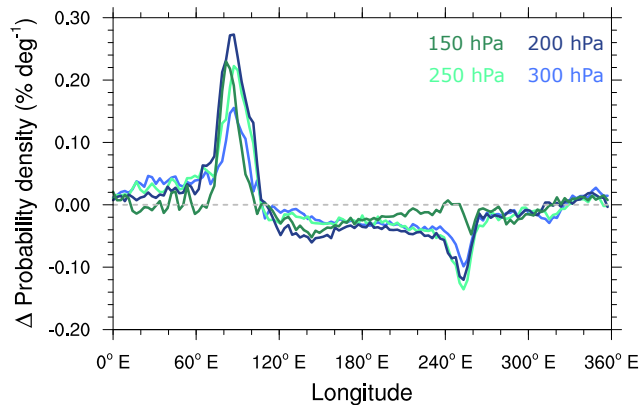
Figure 17. Difference (August minus June) of longitudinal probability densities of parcels that originate from the TP at various pressure
levels in the UT based on 1981–2010 for the LG-D data.

To sum up, we want to point out that the results of EMAC-ATTILA (in particular as they come from a free-running sim-
ulation) should not be seen as validation data but rather as a help to assess which key processes are present in these data as
well. This might help to discern ,which processes/source regions are not heavily dependent on the explicit representation of
465 convection (e.g. through a parametrization) and the detailed meteorology (free-running CCM versus TRJ calculations driven

by reanalysis data). As an example, the contributions from the source regions TP, WP and SEA show similar developments over the course of the monsoon period, although, the quantitative contributions partly differ. Further, the fact that the LG-D and LG-K simulations show discrepancies in parts, e.g. with respect to the mean contributions of the TP of slightly above 14% and 9% (see Fig. 15 and supplement Fig. B3), despite being driven by identical meteorological states of the host model, highlights
470 the influence of the vertical velocity scheme to parts of the analyses. Here, we note that this might be partly already caused by the different distributions of the air parcels in LG-D vs. LG-K data: as the air parcels persist throughout the simulation and are transported with different vertical velocities, the distribution of air parcels within the AMA differs between the two model data sets (see Supplement Fig. B1), even though the same dynamical constraints are used to define the AMA. We are currently planning future work to further carve out the transport properties in the ASM region based on additional Lagrangian CCM
475 simulations.

5 Discussion

5.1 Relation to previous modelling results and observational data

In Section 3 we have presented results regarding PBL to AMA transport based on our trajectory calculation (TRJ). We have found that the boundary layer source distribution (Figs. 4 and 11) focuses over the ASM region (in particular over the Indian subcontinent and the TP). Further, these distributions support previous results regarding the PBL sources of the air masses of the AMA and its surroundings e.g. by Bergman et al. (2013) and Fan et al. (2017). Similarly, the boundary layer crossing distributions are in agreement with convective source maps of the AMA as presented by Legras and Bucci (2020).

Moreover, we found similar regions of upward transport as Bergman et al. (2013), which are located on the south-eastern side of the AMA. However, we also complemented the view about the transport pathways, i.e. the conduit proposed by Bergman et al. (2013), by showing that air masses spread earlier in the AMA volume ~~. In detail, we refined the picture of the vertical conduit by showing that air masses released in the AMA circle within the AMA and fill its three-dimensional structure in~~ in agreement with the ~~slow uplift described by Vogel et al. (2019) and mainly experience upward (downward) transport on the eastern (western) side of the AMA (cf. Fig. 10 presented by Nützel et al., 2016, and discussion by Pan et al., 2016). At lower altitudes where the AMA is weak (or non-existent), vertical transport occurs mainly in (or below) the eastern part of the AMA, in agreement with the regions of upward transport discussed by Bergman et al. (2013). The full pathways (Figs. 6 and 13) are in agreement with the simulated tracer transport shown by Pan et al. (2016, e.g. their Figs. 2 b and c). For CO, a similar distribution in the ASM region was found in model data by Barret et al. (2016), while in their climatological analysis of IASI satellite data the structure was not as conclusive. Using data from the same satellite instrument but performing transient analyses, Luo et al. (2018) came to the conclusion that this transport behaviour is also supported by the satellite data. Similarly, Vogel et al. (2019) noted that the CO transport described by Pan et al. (2016) is in agreement with their results from a trajectory model and MIPAS satellite data. We stress here, that the trace gas results (e.g. in modelling or satellite data) strongly depend also on the strength and location of emissions, whereas the idealized trajectory studies simply track air mass transport.~~ ~~To sum up, these results show~~ transport pathways described by Vogel et al. (2019) and Legras and Bucci (2020). Combining our results with previous studies shows that the transport pathways as diagnosed by (i) a trajectory model including mixing effects (Vogel et al., 2019), (ii) a trajectory model including the effect of observed convection (Legras and Bucci, 2020), (iii) more puristic trajectory models (Bergman et al., 2013, and this study), and (iv) forward trajectories (analyzed backwards in time) from a Lagrangian model with parametrized convection driven by a free-running CCM (this study) are in agreement. Further, the transport pathway is also supported by (v) analyses of CO transport within a CCM and a chemistry-transport model as shown by Pan et al. (2016) and Barret et al. (2016) and (vi) analyses of satellite data (Luo et al., 2018; Vogel et al., 2019). In particular, our results also show that, although there is interannual and strong intraseasonal variability, the main transport characteristics are robust.

Regarding the source regions, our results are in agreement with some of the results found in previous studies, while keeping in mind that there are (sometimes subtle) differences in the study design~~.~~ : As an example, Bergman et al. (2013) found that

roughly 27% of the all trajectories located in the AMA at 200 hPa come from the TP[1], which is similar to the mean contribution of the TP in August in the TRJ data of this study (slightly more than 24%; about 25% for August 2011). The combined area and contribution (again roughly 25% in August; about 26% in August 2011 in the TRJ data) of the regions IND, IP and SEA is comparable to the area and contributions (roughly 32%)[2] of the Asian land masses excluding the TP as analyzed by Bergman et al. (2013).

Further, Vogel et al. (2015) showed contributions of PBL sources to the AMA at 380 K. Although, the TP was not explicitly resolved in their study, the contributions of the source regions used in their study, which cover the TP (red and green lines in their Fig. 8) show a strong increase from June to late July. This increase is in agreement with the increase of the TP contribution found in our study. The dependence of the TP contribution to AMA air masses on the position of the AMA is in analogy to the relation of typhoon–AMA transport discussed by Li et al. (2017), i.e. for the TP or typhoons, entrainment of air masses uplifted from these sources into the core of the AMA depends on the co-location of the AMA and the TP or typhoon, respectively.

Further, the northward shift of the PBL source regions and the transport pathways is consistent with the northward shift of the region of low outgoing longwave radiation and the AMA (Nützel et al., 2016, their Fig. 12; see also the related discussion) and the monsoon (precipitation) itself (e.g. Wang and LinHo, 2002; Yihui and Chan, 2005). This northward propagation can also be seen in deep convective activity as monitored by satellite measurements, where deep convection (up to 150 hPa) over the TP is rare in June and becomes more prominent in July and August (Devasthale and Fueglistaler, 2010).

Goswami et al. (1999) defined an index for the interannual Indian monsoon variability, the so-called monsoon Hadley index (MHI), as meridional wind shear between the UT (200 hPa) and the 850 hPa level over a reference region and motivate their definition by the relation to heating released due to precipitation in the respective region. Here we calculate the MHI from ERA-Interim data based on JJA data. We find that the detrended MHI and (modified) SAHI are strongly anti-correlated (-0.68) over the period 1979–2013 and in particular the anti-correlation for the years where the SAHI is anomalous (i.e. the 14 monsoon seasons for which the backward trajectories have been calculated) is even higher (-0.83). This hints that by analyzing years with rather strong displacements of the AMA to the East or the West, we have implicitly analyzed the impact of the detrended MHI on the transport properties from the PBL to the AMA.

5.2 Uncertainties in the presented results

Despite these agreements, ~~we note that~~ there are some remaining uncertainties with respect to our trajectory calculations. For example, due to the length of our back-trajectory calculations (up to 90 days), individual trajectories must not be analyzed, nevertheless, statistical analyses are possible as noted by Bergman et al. (2013).

---

[1]Here we refer to the 1 degree data results of (Bergman et al., 2013) who find that about 35% of the PBL crossing trajectories, which in turn correspond to roughly 78% of all trajectories starting in the AMA come from the TP in August 2011. This translates to an approximate contribution of the TP air masses to the AMA of about 27%.

[2]As for the TP contribution the 1 degree values presented by Bergman et al. (2013) have been converted to contributions regarding all trajectories starting within the AMA.

~~We further acknowledge that~~ Further, the TRJ calculations do not feature explicit convection. With respect to the importance of convection, Wu et al. (2020) showed with a free-running CCM that for the first uplift in the ASM region convection is dominant but in the UTLS the large scale dynamics are most relevant for the tracer budget. A recent study by Smith et al. (2021) investigated how convective processes are captured in the vertical velocity field of (re)analysis data. They came to the conclusion that kinematic trajectories based on (re)analyses winds incorporate the effects of convection to a substantial degree. However, they also noted that higher temporal and spatial resolution, e.g. as in ERA5 (Hersbach et al., 2020), seems to be favourable for the inclusion of convective effects. Using the same modelling approach as in the present study, Bergman et al. (2013) showed that their results from the kinematic trajectories regarding source region contributions are relatively robust with respect to the choice of the resolution of the input data, which lends credit to their and also to our results. Further, they also found that the vertical velocity of the (re)analysis data is correlated with observed precipitation data, which in turn is related to convective activity.

To assess the possible sensitivity of our results to missing convection, we ~~also~~ presented results from a free-running CCM with Lagrangian transport and a Lagrangian convection parametrization, namely EMAC-ATTILA. ~~These results suggest that seasonal evolutions of some~~ For some of the source regions (e.g. SEA and WP), the seasonal evolutions are supported by the EMAC-ATTILA data ~~and in particular~~. In particular, the increase of the TP contribution to the AMA air masses is also present in ~~these~~ the EMAC-ATTILA data. This in turn indicates that for a qualitative description of the contribution of these PBL source regions the explicit representation of convection might not be essential. Nevertheless, ~~in particular~~ the fastest transport from the PBL to the upper troposphere might be underestimated in our TRJ data (cf. Figs. 6 and B2 - showing that trajectories are transported faster upward in the the EMAC-ATTILA data).

5.3 Contribution of the TP

We note that we investigated transport from the top of the PBL to the AMA, i.e. our analyses end at the top of the PBL. Convergence of surface winds at the southern flank of the TP (Pan et al., 2016, their Fig. 8) might cause low level transport of emissions from their source regions to the final exit and uplift region from the PBL to the AMA. As an example, emissions e.g. of CO are low over the TP (Park et al., 2009; Barret et al., 2016, their Figs. 9 and 10, respectively), nevertheless air masses transported from the PBL over the TP to the AMA can carry considerable CO signatures (Pan et al., 2016, their Figs. 2b and 7).

Independently of potential limitations in the TRJ or EMAC-ATTILA data, the increase of TP air masses to the AMA composition is also backed up by ERA-Interim data, which is shown in Fig. 18: In May the core of the subtropical jet is located right above the TP. During the course of the monsoon season, the tropical easterly jet, which is located on the southern boundary of the AMA (Dethof et al., 1999), strengthens. This indicates an increase of the anticyclonic circulation of the AMA. Further, the subtropical jet - which is located on the northern boundary of the AMA (Dethof et al., 1999) - as well as the zero-wind line move northward. Consequently, air masses that are transported upward from the TP are likely to be advected by the subtropical westerly jet during the early phase of the monsoon season (June), while they can feed into the core of the AMA during August.
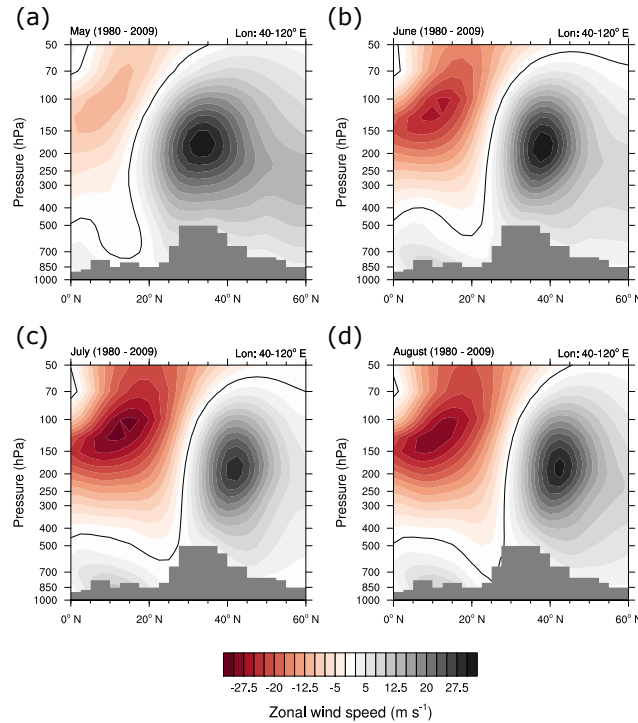
Figure 18. Zonal winds from ERA-Interim for **(a)** May to **(d)** August averaged over 1980 to ~~2009.~~ 2009 and 40-120° E. Red (grey) colours indicate westward (eastward) winds and black contours indicate the zero-wind line. Grey shadings mark orography.

~~In this study, we investigated transport from the top of the PBL to the AMA, i.e. our analyses end at the top of the PBL. Convergence of surface winds at the southern flank of the TP (Pan et al., 2016, their Fig. 8) might cause low level transport of emissions from their source regions to the final exit and uplift region from the PBL to the AMA. As an example, emissions~~
575 ~~e.g. of CO are low over the TP (Park et al., 2009; Barret et al., 2016, their Figs. 9 and 10, respectively), nevertheless air masses transported from the PBL over the TP to the AMA can carry considerable CO signatures (Pan et al., 2016, their Figs. 2b and 7). This issue is common to many of the previous studies regarding the source regions of AMA air masses and could be overcome by employing surface emissions, which would lead to an analysis of the efficiency of transport to the AMA as noted already for the use of forward trajectories by Bergman et al. (2013).~~

580   Finally, as Bergman et al. (2013) found a relatively large contribution of air masses from the TP to the AMA, they discuss their results in relation to other studies that either do or do not find important contributions of the TP to the air masses (or tracer fields) in the AMA or UTLS. While they correctly argue that the results strongly depend on the chosen analysis method, we ~~can add another possible explanation for these differences~~ want to add that the strong intraseasonal variability might be a reason for the differences with respect to the TP contribution: Most of the studies that find strong contributions of the TP to the
585 AMA or UTLS focus on August conditions e.g. Fu et al. (2006), Bergman et al. (2013) and Jensen et al. (2015).

In contrast, Park et al. (2009) investigated the source region contribution and transport budget of CO to the AMA and came to the conclusion that the TP has a relatively low impact on the CO maximum in the AMA region. For the source region contribution, i.e. the contribution of CO emitted from the TP, they showed that the lack of surface emissions from the TP leads to this minor impact. In a vertically resolved CO budget analysis for the TP region they found that convection leads to a small maximum around 400 hPa while advection leads to a negative tendency in the middle troposphere and thus argued that the TP does not play an important role with respect to CO transport to the AMA. The negative advection tendency found in their analysis is most likely related to the location of the subtropical jet over the TP in June 2005, which might have caused air masses to be transported out of the TP region. In our analyses, the contribution from the TP to air masses within the AMA increases as the subtropical jet shifts northwards from June to August and we find, that the transport of TP boundary layer air out of the AMA region decreases accordingly (see Fig. 17).

Further, Devasthale and Fueglistaler (2010) put the importance of TP convection into perspective, however, they also showed that deep convective activity over the TP increases from June to August (see their Fig. 3). Similarly, from the convective upward mass flux in the EMAC-ATTILA data, we find that in July and August the mass flux into the upper troposphere (above ∼350 hPa) over the TP is larger than in June (not shown). ~~Hence, these previous results might also be strongly influenced by the different analysis periods.~~

6 Summary and conclusion

In this study we have analyzed the transport pathways and source regions from the PBL to the AMA. This was achieved by calculating trajectories for 14 monsoon seasons using reanalysis wind fields. Additional results from 30 monsoon seasons from a Lagrangian transport model, which was run within a free-running CCM, were used to confirm these results. The presented analyses (Sects.3 and 4) and the discussion in the previous section (Sect.5) allow us to ~~draw the following conclusions~~ answer the following questions regarding the transport characteristics of air masses from the PBL to the AMA.

1. What is the climatological perspective of PBL to AMA transport in terms of pathways and PBL source regions? How reliable are previous results?

   – Our results show that during JJA on a climatological basis, AMA air mass ~~sources~~ come from a broad region in the PBL in Asia~~and with~~. With increasing height, the upward transport of air masses focuses on the eastern side of (or below) the AMA. However, ~~by construction this analysis only captures the regions of upward transport to the AMA and not necessarily the full three-dimensional pathways. The main upward transport occurs on the eastern side below the anticyclone. We~~ we found an upward circling already considerably below 150 hPa for ~~some of the trajectories. This result refines the original conduit schematic as depicted and discussed by Bergman et al. (2013) and is in full accordance with the large scale uplift above 360 K described by Vogel et al. (2019).~~

approximately half of the PBL crossing trajectories. The attribution of PBL source regions, however, is less clear. In TRJ, the largest contributions from the named source regions are found from the TP region (around 17%), the IND region (around 13%) and the WP region (around 12%). In LG-D we find almost the same contribution from the TP (15%) and the WP (12%), however the contribution from IND and SEA are the largest. ~~This might be related to a large convective contribution, which is missing in TRJ. This could also imply that the convective contribution from WP is small, because both methods show the same contribution from WP. The LG-K results are similar to LG-D, but show a smaller contribution of the TP (9%).~~

2. How do the pathways and source regions vary on intraseasonal and interannual time scales?

   – ~~With respect to the transport pathways, we~~ We find that the qualitative behaviour of the transport pathways is similar throughout the monsoon season and between different monsoon seasons, i.e. upward transport on the eastern side below the AMA and subsequent upward transport within the AMA. Nevertheless, in particular with respect to the intraseasonal variation, the transport pathways shift considerably northwards over the course of the monsoon season in accordance with the shift of the monsoon system. ~~With respect to the source regions, we~~ Further, we also find strong interannual and intraseasonal variability with respect to the PBL source region contributions. For the latter, the contribution from the TP, which strongly increases from around 2% (4%) in TRJ (LG-D) in early June to around 24% (20%) in TRJ (LG-D) in early August, sticks out. This increase is ~~in agreement with corresponding reanalyses data of the subtropical jet position. Considering the variability of the AMA is thus a potential starting point for reconciling~~ (partly) related to the relative position of the AMA and the subtropical jet. We show that taking the strong interaseasonal variability into account can help to reconcile differences in previous studies ~~on~~ concerning PBL to AMA transport, in particular with respect to the ~~impact~~ contribution of the TP.

3. Are the PBL source regions and the transport pathways related to interannual east-west shifts of the AMA?

   – We ~~find~~ identify shifts in the transport pathways between east and west years, although the main characteristics are qualitatively unchanged. Further, we ~~find~~ show that the longitudinal shifts of the AMA are related to the so-called monsoon Hadley-Index. For the PBL sources we find no considerable differences between east and west years with respect to the defined source regions, while a map shows that there are (small) regional shifts in the contribution of the PBL sources.

From our results we find that the three-dimensional pathways of trajectories give a conclusive picture of transport from the PBL to the AMA. However, the relative contribution from the PBL source regions are (except for TP and WP) less robust. In our analysis we could not distinguish, whether the differences in source region contribution are a result of the different synoptic conditions in the free-running EMAC-ATTILA simulation compared to the reanalysis driven TRJ calculations or actually a result of the consideration of Lagrangian convection in the EMAC-ATTILA data. A first indication of faster vertical transport due to parametrized convection in the LG data comes from the observation that a lower fraction of trajectories do not encounter

the PBL in the LG simulations compared to the TRJ-data.

650

To allow for a more robust picture of the transport from the PBL to the AMA in the monsoon region, further investigations with various model setups would be beneficial. In particular, a set of tailored simulations with and without convective transport would be valuable to assess the impact of convective transport with respect to individual source region contributions to AMA air masses.

Data availability. ERA-Interim data is available from the European Centre for Medium-Range Weather Forecast (ECMWF) (2011): (i) Copyright statement: Copyright "© [2022] European Centre for Medium-Range Weather Forecasts (ECMWF)". (ii) Source: www.ecmwf.int, (iii) Licence Statement: This data is published under a Creative Commons Attribution 4.0 International (CC BY 4.0). https://creativecommons. org/licenses/by/4.0/. (iv) Disclaimer: ECMWF does not accept any liability whatsoever for any error or omission in the data, their availability, or for any loss or damage arising from their use. (v) Where applicable, an indication if the material has been modified and an indication of previous modifications: The trajectory data (TRJ) was derived using ERA-Interim data (ECMWF,2011). Further, additional analyses are based on ERA-Interim data.

Appendix A

A1 ~~EMAC-ATTILA setup details~~

~~In the following, we provide a more detailed description of the EMAC-ATTILA simulation setup used in this study. This description is largely based on the description by (Brinkop and Jöckel, 2019) and we refer the reader to their publication for further details.~~

~~EMAC consists of the ECHAM5 (European Centre HAMburg general circulation model version 5; Roeckner et al., 2003, 2006) model and the MESSy infrastructure (Modular Earth Submodel System Jöckel et al., 2005, 2010). Within EMAC, the submodel ATTILA (see Reithmeier and Sausen, 2002, for the original model description) can be used to calculate Lagrangian transport of air parcels (Brinkop and Jöckel, 2019). The simulations employed here are based on MESSy version 2.53 (corresponding updates will be available in version 2.55) and are dubbed LG(diab) and LG(kin), respectively by (Brinkop and Jöckel, 2019). We note that technically data from LG-D and LG-K were obtained from two different simulations, however the driving grid point meteorology was identical in both cases (Brinkop and Jöckel, 2019).~~

~~Based on the description by Brinkop and Jöckel (2019) we present the most important aspects of these simulations here as well: The simulations feature a spectral truncation for the ECHAM5 base model of T42 (corresponding to a quadratic Gaussian grid of ~2.8° x 2.8°) in the middle atmosphere (MA) setup with 47 model levels up to ~0.01 hPa, i.e. the so-called T42L47MA setup. In the free-running, i.e. no nudging of dynamic variables, EMAC-ATTILA simulations exploited here, radiatively active trace gases have been prescribed from a previous simulation with full chemistry (RC1-base08 described by Jöckel et al., 2016) to reduce the computational effort. Only a chemistry scheme for methane oxidation, the CH4 submodel (Winterstein and Jöckel, 2021), was turned on to allow for the feedback on stratospheric water vapour. Sea surface temperatures and sea ice cover in these simulations were prescribed from HadISST (Rayner et al., 2003).~~

A1 AMA boundary determination

In this study mostly trajectories starting within the core of the AMA have been analyzed. The determination of the boundary of the AMA is difficult and many studies have used various quantities and thresholds to determine the boundary of the AMA (e.g. Park et al., 2007; Garny and Randel, 2013; Ploeger et al., 2015; Santee et al., 2017). Here, the boundary determination is based on a geopotential height anomaly (GPHA) threshold as proposed by Barret et al. (2016). They calculated GPHAs with respect

to the 50° S-50° N mean and used a threshold of 270 m for the pressure levels 100, 150 and 200 hPa based on previously used boundaries. For our data, we have derived thresholds explicitly for the trajectory model calculations using ERA-Interim data at 2.5 degree grid spacing and for the EMAC-ATTILA simulations using the CCM grid point data. In principal, we have deter-

690 mined suitable threshold candidates by ~~producing scatter plots of the geopotential height anomaly and the maximum meridional wind strength along the ridge-line of the AMA (see Zhang et al., 2002, for the ridge-line definition)~~ deriving a single GPHA value, which on average represents the strongest anticyclonic circulation. This was done by calculating the mean of the GPHA values associated with the strongest meridional winds (southward and northward) along the ridge line (see Zhang et al., 2002, for the ridge l For EMAC-ATTILA, we further required the maximum wind speed to be located at a grid point with GPHA of at least 100 m

695 to avoid noise from unrealistically low values. Using this technique, we determined anomaly thresholds of 280 m and 295 m for ERA-Interim and EMAC-ATTILA data, respectively. The value of 280 m for ERA-Interim is in good agreement with the threshold of 270 m used by Barret et al. (2016).

A2   Selection of summer seasons for the TRJ calculations

The trajectory model calculations described in Sect. 2 have been performed for 14 NH-summer seasons in the period 1979–

700 2013. These NH-summers have been selected as the mean position of the AMA was rather displaced to the East or West. In detail, a modified version of the South Asian High Index (SAHI), which was originally defined by Wei et al. (2014), has been used. Wei et al. (2014) calculated the SAHI by standardizing the time series of differences of geopotential height over a box in the east of the AMA (22.5-32.5°N x 85-105°E) minus that over a box in the west of the AMA (22.5-32.5°N x 55-75°E) at a single pressure level. Compared to the definition by Wei et al. (2014), we use a modified version, which standardizes the

705 sums of these differences over three pressure levels (100, 150 and 200 hPa). We use these pressure levels as they are centered around the starting level of the trajectories (150 hPa). ERA-Interim data with a grid spacing of 2.5° x 2.5° have been used to determine the modified SAHI and using a threshold of ±0.7 deviation from the mean we found fourteen years with a rather eastward or westward displaced AMA (seven years each).[3] The corresponding starting probabilities for the east (cyan) and west (~~purple~~magenta) composites are shown in Fig. 3.

710 **Appendix B: Supplemental figures**

---

[3]West years: 1980, 1984, 1994, 2001, 2007, 2008 and 2011 – East years: 1981, 1987, 1989, 1998, 2009, 2010 and 2012.
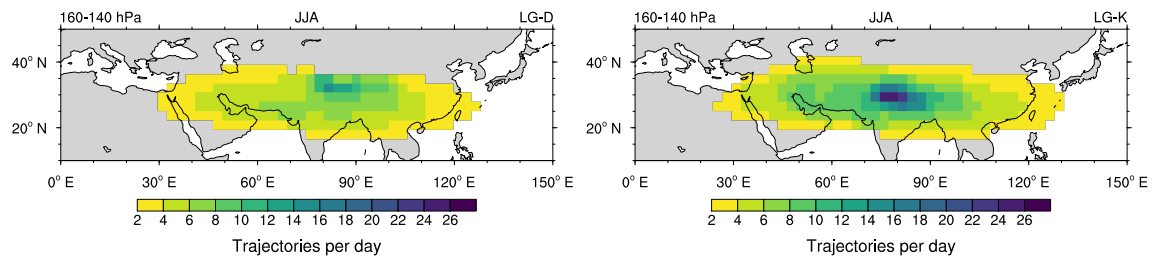
Figure B1. Starting frequency of trajectories for LG-D (left) and LG-K (right) over the years 1981-2010. For LG-K data for 2008 was removed - see text for details.
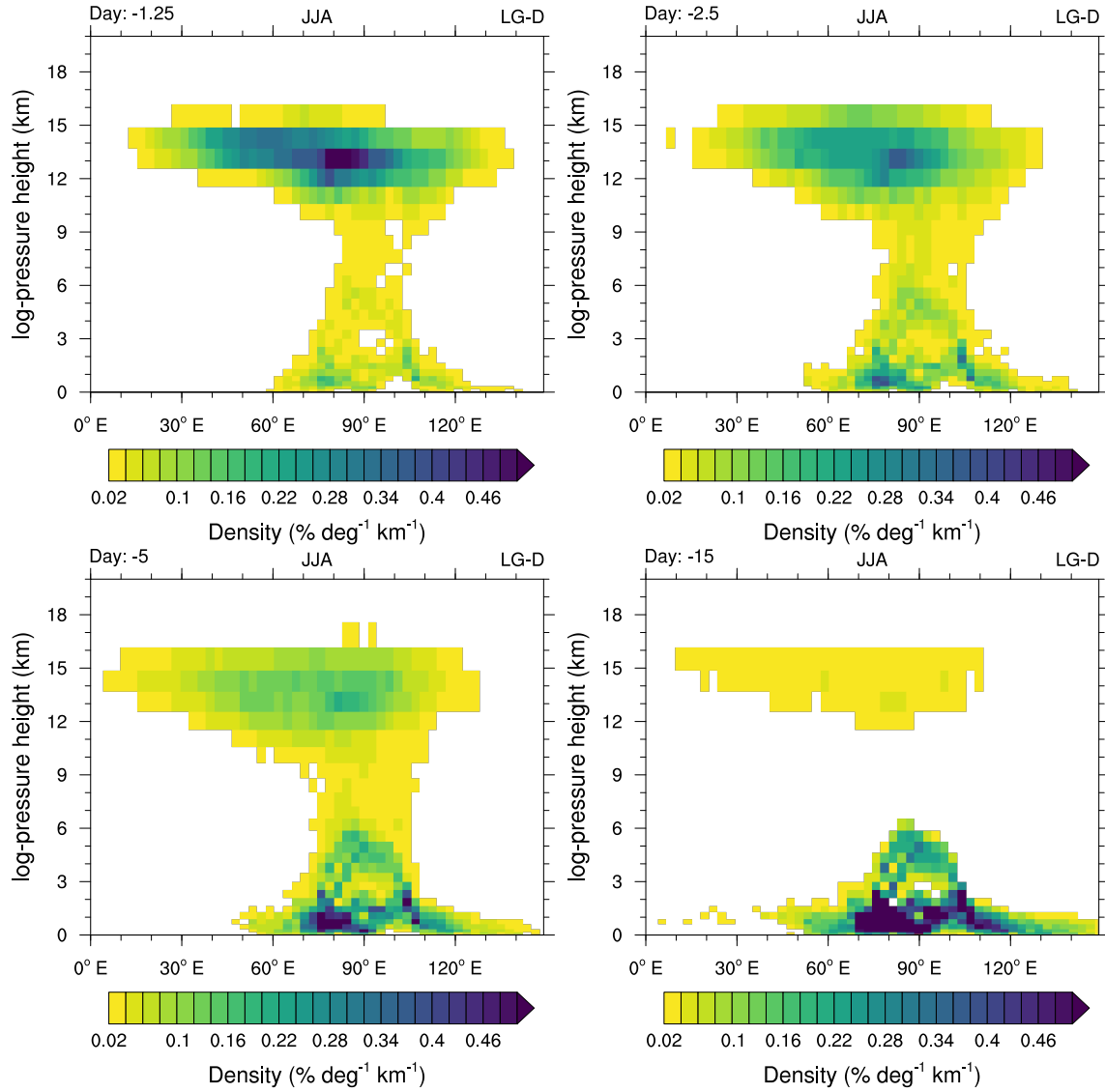
Figure B2. Density of trajectory distributions integrated over 0-50° N as in Fig 6 but for the LG-D data from 1981-2010 for 1.25, 2.5, 5 and 15 days prior to the arrival of the trajectories in the AMA at approximately 150 hPa.
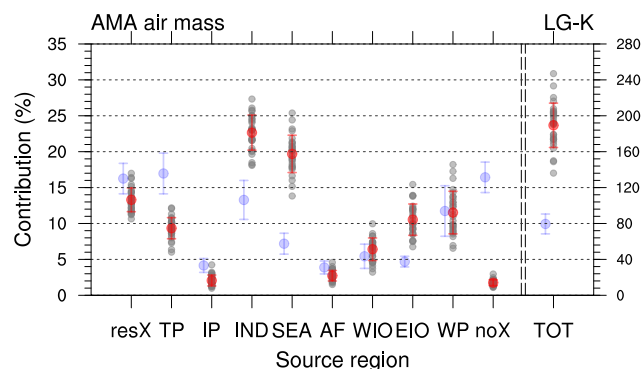
Figure B3. Contributions of PBL sources to the AMA around 150 hPa for the LG-K simulation for 1981-2010 (with 2008 removed, see text for details). ~~Whiskers~~ Mean values are given as red dots, red whiskers denote the interannual standard deviation ~~, whereas~~ and individual years are indicated via grey dots. For TOT ~~1% corresponds to 8000~~ the right axis denotes the total number of trajectories in units of 10^3 trajectories. For comparison faint blue dots and whiskers denote the values from the TRJ data.
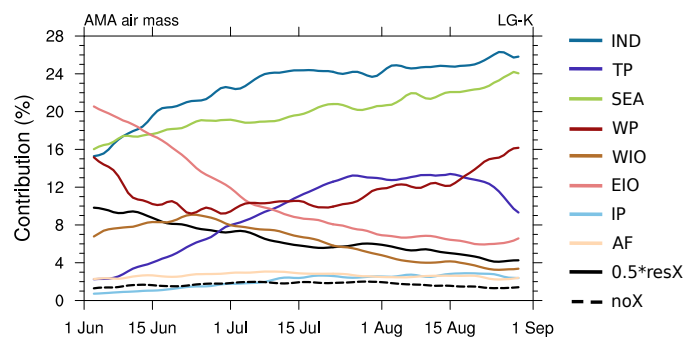
Figure B4. Source evolution in the LG-K data during 1981 to 2010 (with 2008 removed, see text for details). resX data has been scaled by 0.5. All contributions have been smoothed via 5 day running means (weights of $[\frac{1}{9}, \frac{2}{9}, \frac{3}{9}, \frac{2}{9}, \frac{1}{9}]$), while daily data were produced from summing up the ten hourly data for each day.

Note: Fig. B4 slightly updated compared to the diff-version in the author comments

Author contributions. Large parts of the work presented here - in particular the kinematitc trajectory analyses - are based on work performed for the PhD thesis of MN. The presented analyses have been performed by MN with help of SB for postprocessing of the EMAC-ATTILA data. The EMAC-ATTILA simulations were performed by SB and PJ. The manuscript was mainly composed by MN, while all authors contributed to the writing and discussion.

Competing interests. In accordance with the competing interest policy of Copernicus Publications, we note that two (or more) co-authors are members of the editorial board of ACP. The authors declare that no other conflict of interest is present.

Acknowledgements. We thank the two anonymous reviewers and Helmut Ziereis (DLR) for comments on their comments, which helped to improve the manuscript. We thank the ECMWF for producing and distributing ERA-Interim reanalysis data. EMAC-ATTILA data were produced and analyzed at the Leibniz-Rechenzentrum in Garching, Germany. The authors gratefully acknowledge the Gauss Centre for Supercomputing e.V. (www.gauss-centre.eu) for funding this project by providing computing time on the GCS Supercomputer SuperMUC-NG at Leibniz Supercomputing Centre (www.lrz.de). CDO (Climate Data Operators) was used for data processing (available at https://code.mpimet.mpg.de/projects/cdo/, last access: 24 Jan. 2022; Schulzweida, 2021)). We used the NCAR Command Language (NCL, 2019, see references) for data analysis, processing and graphics.

Financial support. The research leading to these results has received funding from the European Community's Seventh Framework Programme (FP7/2007–2013) under grant agreement no. 603557. The work described in this paper has received funding from the Initiative and Networking Fund of the Helmholtz Association through the project "Advanced Earth System Modelling Capacity (ESM)". The content of the paper is the sole responsibility of the author(s) and it does not represent the opinion of the Helmholtz Association, and the Helmholtz Association is not responsible for any use that might be made of the information contained. HG was funded by the Helmholtz Association under grant no. VH-NG-1014 (Helmholtz Young Investigators Group MACClim). M. Park acknowledges support from the NASA's Aura Science Team Program (NNH19ZDA001N-0030). L. Pan acknowledges support from the US National Science Foundation (NSF) through the funding of National Center for Atmospheric Research (NCAR) operation, grant AGS-1852977.

References

Abalos, M., Randel, W. J., Kinnison, D. E., and Garcia, R. R.: Using the Artificial Tracer e90 to Examine Present and Future UTLS Tracer Transport in WACCM, Journal of the Atmospheric Sciences, 74, 3383 – 3403, https://doi.org/10.1175/JAS-D-17-0135.1, 2017.

Barret, B., Sauvage, B., Bennouna, Y., and Le Flochmoen, E.: Upper-tropospheric CO and O_3 budget during the Asian summer monsoon, Atmospheric Chemistry and Physics, 16, 9129–9147, https://doi.org/10.5194/acp-16-9129-2016, 2016.

Bergman, J. W., Fierli, F., Jensen, E. J., Honomichl, S., and Pan, L. L.: Boundary layer sources for the Asian anticyclone: Regional contributions to a vertical conduit, J. Geophys. Res.-Atmos., 118, 2560–2575, https://doi.org/10.1002/jgrd.50142, 2013.

Brinkop, S. and Jöckel, P.: ATTILA 4.0: Lagrangian advective and convective transport of passive tracers within the ECHAM5/MESSy (2.53.0) chemistry–climate model, Geoscientific Model Development, 12, 1991–2008, https://doi.org/10.5194/gmd-12-1991-2019, 2019.

Brunamonti, S., Jorge, T., Oelsner, P., Hanumanthu, S., Singh, B. B., Kumar, K. R., Sonbawne, S., Meier, S., Singh, D., Wienhold, F. G., Luo, B. P., Boettcher, M., Poltera, Y., Jauhiainen, H., Kayastha, R., Karmacharya, J., Dirksen, R., Naja, M., Rex, M., Fadnavis, S., and Peter, T.: Balloon-borne measurements of temperature, water vapor, ozone and aerosol backscatter on the southern slopes of the Himalayas during StratoClim 2016–2017, Atmospheric Chemistry and Physics, 18, 15 937–15 957, https://doi.org/10.5194/acp-18-15937-2018, 2018.

Bucci, S., Legras, B., Sellitto, P., D'Amato, F., Viciani, S., Montori, A., Chiarugi, A., Ravegnani, F., Ulanovsky, A., Cairo, F., and Stroh, F.: Deep-convective influence on the upper troposphere–lower stratosphere composition in the Asian monsoon anticyclone region: 2017 StratoClim campaign results, Atmospheric Chemistry and Physics, 20, 12 193–12 210, https://doi.org/10.5194/acp-20-12193-2020, 2020.

Chen, B., Xu, X. D., Yang, S., and Zhao, T. L.: Climatological perspectives of air transport from atmospheric boundary layer to tropopause layer over Asian monsoon regions during boreal summer inferred from Lagrangian approach, Atmospheric Chemistry and Physics, 12, 5827–5839, https://doi.org/10.5194/acp-12-5827-2012, 2012.

Dee, D. P., Uppala, S. M., Simmons, A. J., Berrisford, P., Poli, P., Kobayashi, S., Andrae, U., Balmaseda, M. A., Balsamo, G., Bauer, P., Bechtold, P., Beljaars, A. C. M., van de Berg, L., Bidlot, J., Bormann, N., Delsol, C., Dragani, R., Fuentes, M., Geer, A. J., Haimberger, L., Healy, S. B., Hersbach, H., Hólm, E. V., Isaksen, L., Kållberg, P., Köhler, M., Matricardi, M., McNally, A. P., Monge-Sanz, B. M., Morcrette, J.-J., Park, B.-K., Peubey, C., de Rosnay, P., Tavolato, C., Thépaut, J.-N., and Vitart, F.: The ERA-Interim reanalysis: configuration and performance of the data assimilation system, Q. J. Roy. Meteor. Soc., 137, 553–597, https://doi.org/10.1002/qj.828, 2011.

Dethof, A., Oneill, A., Slingo, J. M., and Smit, H. G. J.: A mechanism for moistening the lower stratosphere involving the Asian summer monsoon, Q. J. Roy. Meteor. Soc., 125, 1079–1106, https://doi.org/10.1256/smsqj.55601, 1999.

Devasthale, A. and Fueglistaler, S.: A climatological perspective of deep convection penetrating the TTL during the Indian summer monsoon from the AVHRR and MODIS instruments, Atmospheric Chemistry and Physics, 10, 4573–4582, https://doi.org/10.5194/acp-10-4573-2010, 2010.

Ding, Y.: The Variability of the Asian Summer Monsoon, Journal of the Meteorological Society of Japan. Ser. II, 85B, 21–54, https://doi.org/10.2151/jmsj.85B.21, 2007.

European Centre for Medium-Range Weather Forecast (ECMWF): The ERA-Interim reanalysis dataset, Copernicus Climate Change Service (C3S) (last accessed 10-2021), https://www.ecmwf.int/en/forecasts/datasets/archive-datasets/reanalysis-datasets/era-interim, 2011.

Fan, Q.-J., Bian, J.-C., and Pan, L. L.: Atmospheric boundary layer sources for upper tropospheric air over the Asian summer monsoon region, Atmospheric and Oceanic Science Letters, 10, 358–363, https://doi.org/10.1080/16742834.2017.1344089, 2017.

Fu, R., Hu, Y., Wright, J. S., Jiang, J. H., Dickinson, R. E., Chen, M., Filipiak, M., Read, W. G., Waters, J. W., and Wu, D. L.: Short circuit of water vapor and polluted air to the global stratosphere by convective transport over the Tibetan Plateau, Proceedings of the National Academy of Sciences, 103, 5664–5669, https://doi.org/10.1073/pnas.0601584103, 2006.

770 Garny, H. and Randel, W. J.: Dynamic variability of the Asian monsoon anticyclone observed in potential vorticity and correlations with tracer distributions, J. Geophys. Res.-Atmos., 118, 13 421–13 433, https://doi.org/10.1002/2013JD020908, 2013.

Garny, H. and Randel, W. J.: Transport pathways from the Asian monsoon anticyclone to the stratosphere, Atmospheric Chemistry and Physics, 16, 2703–2718, https://doi.org/10.5194/acp-16-2703-2016, 2016.

Goswami, B. N., Krishnamurthy, V., and Annmalai, H.: A broad-scale circulation index for the interannual variability of the Indian summer 775 monsoon, Quarterly Journal of the Royal Meteorological Society, 125, 611–633, https://doi.org/https://doi.org/10.1002/qj.49712555412, 1999.

Heath, N. K. and Fuelberg, H. E.: Using a WRF simulation to examine regions where convection impacts the Asian summer monsoon anticyclone, Atmos. Chem. Phys., 14, 2055–2070, https://doi.org/10.5194/acp-14-2055-2014, 2014.

Hersbach, H., Bell, B., Berrisford, P., Hirahara, S., Horányi, A., Muñoz-Sabater, J., Nicolas, J., Peubey, C., Radu, R., Schepers, D., Sim- 780 mons, A., Soci, C., Abdalla, S., Abellan, X., Balsamo, G., Bechtold, P., Biavati, G., Bidlot, J., Bonavita, M., De Chiara, G., Dahlgren, P., Dee, D., Diamantakis, M., Dragani, R., Flemming, J., Forbes, R., Fuentes, M., Geer, A., Haimberger, L., Healy, S., Hogan, R. J., Hólm, E., Janisková, M., Keeley, S., Laloyaux, P., Lopez, P., Lupu, C., Radnoti, G., de Rosnay, P., Rozum, I., Vamborg, F., Villaume, S., and Thépaut, J.-N.: The ERA5 global reanalysis, Quarterly Journal of the Royal Meteorological Society, 146, 1999–2049, https://doi.org/https://doi.org/10.1002/qj.3803, 2020.

785 Honomichl, S. B. and Pan, L. L.: Transport From the Asian Summer Monsoon Anticyclone Over the Western Pacific, Journal of Geophysical Research: Atmospheres, 125, e2019JD032 094, https://doi.org/10.1029/2019JD032094, e2019JD032094 2019JD032094, 2020.

Hoskins, B. J. and Rodwell, M. J.: A Model of the Asian Summer Monsoon. Part I: The Global Scale, J. Atmos. Sci., 52, 1329–1340, https://doi.org/10.1175/1520-0469(1995)052<1329:AMOTAS>2.0.CO;2, 1995.

Jensen, E. J., Pfister, L., Ueyama, R., Bergman, J. W., and Kinnison, D.: Investigation of the transport processes controlling the geo- 790 graphic distribution of carbon monoxide at the tropical tropopause, Journal of Geophysical Research: Atmospheres, 120, 2067–2086, https://doi.org/10.1002/2014JD022661, 2014JD022661, 2015.

Jöckel, P., Sander, R., Kerkweg, A., Tost, H., and Lelieveld, J.: Technical Note: The Modular Earth Submodel System (MESSy) - a new approach towards Earth System Modeling, Atmos. Chem. Phys., 5, 433–444, https://doi.org/10.5194/acp-5-433-2005, 2005.

Jöckel, P., Kerkweg, A., Pozzer, A., Sander, R., Tost, H., Riede, H., Baumgaertner, A., Gromov, S., and Kern, B.: Development cycle 2 of the 795 Modular Earth Submodel System (MESSy2), Geoscientific Model Development, 3, 717–752, https://doi.org/10.5194/gmd-3-717-2010, 2010.

Jöckel, P., Tost, H., Pozzer, A., Kunze, M., Kirner, O., Brenninkmeijer, C. A. M., Brinkop, S., Cai, D. S., Dyroff, C., Eckstein, J., Frank, F., Garny, H., Gottschaldt, K.-D., Graf, P., Grewe, V., Kerkweg, A., Kern, B., Matthes, S., Mertens, M., Meul, S., Neumaier, M., Nützel, M., Oberländer-Hayn, S., Ruhnke, R., Runde, T., Sander, R., Scharffe, D., and Zahn, A.: Earth System Chemistry integrated Mod- 800 elling (ESCiMo) with the Modular Earth Submodel System (MESSy) version 2.51, Geoscientific Model Development, 9, 1153–1200, https://doi.org/10.5194/gmd-9-1153-2016, 2016.

Krishnamurti, T. N. and Bhalme, H. N.: Oscillations of a Monsoon System. Part I. Observational Aspects, Journal of Atmospheric Sciences, 33, 1937 – 1954, https://doi.org/10.1175/1520-0469(1976)033<1937:OOAMSP>2.0.CO;2, 1976.

Legras, B. and Bucci, S.: Confinement of air in the Asian monsoon anticyclone and pathways of convective air to the stratosphere during the summer season, Atmospheric Chemistry and Physics, 20, 11 045–11 064, https://doi.org/10.5194/acp-20-11045-2020, 2020.

Li, D., Vogel, B., Bian, J., Müller, R., Pan, L. L., Günther, G., Bai, Z., Li, Q., Zhang, J., Fan, Q., and Vömel, H.: Impact of typhoons on the composition of the upper troposphere within the Asian summer monsoon anticyclone: the SWOP campaign in Lhasa 2013, Atmospheric Chemistry and Physics, 17, 4657–4672, https://doi.org/10.5194/acp-17-4657-2017, 2017.

Luo, J., Pan, L. L., Honomichl, S. B., Bergman, J. W., Randel, W. J., Francis, G., Clerbaux, C., George, M., Liu, X., and Tian, W.: Space–time variability in UTLS chemical distribution in the Asian summer monsoon viewed by limb and nadir satellite sensors, Atmospheric Chemistry and Physics, 18, 12 511–12 530, https://doi.org/10.5194/acp-18-12511-2018, 2018.

Mason, R. B. and Anderson, C. E.: The development and decay of the 100-mb. summertime anticyclone over southern Asia, Mon. Weather Rev., 91, 3–12, https://doi.org/10.1175/1520-0493(1963)091<0003:TDADOT>2.3.CO;2, 1963.

NCL: The NCAR Command Language (Version 6.6.2) [Software], UCAR/NCAR/CISL/TDD, Boulder, Colorado, https://doi.org/10.5065/D6WD3XH5, 2019.

Nützel, M., Dameris, M., and Garny, H.: Movement, drivers and bimodality of the South Asian High, Atmos. Chem. Phys., 16, 14 755–14 774, https://doi.org/10.5194/acp-16-14755-2016, 2016.

Nützel, M., Podglajen, A., Garny, H., and Ploeger, F.: Quantification of water vapour transport from the Asian monsoon to the stratosphere, Atmospheric Chemistry and Physics, 19, 8947–8966, https://doi.org/10.5194/acp-19-8947-2019, 2019.

Pan, L. L., Honomichl, S. B., Kinnison, D. E., Abalos, M., Randel, W. J., Bergman, J. W., and Bian, J.: Transport of chemical tracers from the boundary layer to stratosphere associated with the dynamics of the Asian summer monsoon, Journal of Geophysical Research: Atmospheres, 121, 14,159–14,174, https://doi.org/10.1002/2016JD025616, 2016JD025616, 2016.

Park, M., Randel, W. J., Gettelman, A., Massie, S. T., and Jiang, J. H.: Transport above the Asian summer monsoon anticyclone inferred from Aura Microwave Limb Sounder tracers, J. Geophys. Res.-Atmos., 112, D16 309, https://doi.org/10.1029/2006JD008294, 2007.

Park, M., Randel, W. J., Emmons, L. K., and Livesey, N. J.: Transport pathways of carbon monoxide in the Asian summer monsoon diagnosed from Model of Ozone and Related Tracers (MOZART), J. Geophys. Res.-Atmos., 114, D08 303, https://doi.org/10.1029/2008JD010621, 2009.

Ploeger, F., Gottschling, C., Griessbach, S., Grooß, J.-U., Guenther, G., Konopka, P., Müller, R., Riese, M., Stroh, F., Tao, M., Ungermann, J., Vogel, B., and von Hobe, M.: A potential vorticity-based determination of the transport barrier in the Asian summer monsoon anticyclone, Atmos. Chem. Phys., 15, 13 145–13 159, https://doi.org/10.5194/acp-15-13145-2015, 2015.

Ploeger, F., Konopka, P., Walker, K., and Riese, M.: Quantifying pollution transport from the Asian monsoon anticyclone into the lower stratosphere, Atmospheric Chemistry and Physics, 17, 7055–7066, https://doi.org/10.5194/acp-17-7055-2017, 2017.

Randel, W. J. and Park, M.: Deep convective influence on the Asian summer monsoon anticyclone and associated tracer variability observed with Atmospheric Infrared Sounder (AIRS), J. Geophys. Res., 111, D12 314, https://doi.org/10.1029/2005JD006490, 2006.

Randel, W. J., Park, M., Emmons, L., Kinnison, D., Bernath, P., Walker, K. A., Boone, C., and Pumphrey, H.: Asian Monsoon Transport of Pollution to the Stratosphere, Science, 328, 611–613, https://doi.org/10.1126/science.1182274, 2010.

Rayner, N. A., Parker, D. E., Horton, E. B., Folland, C. K., Alexander, L. V., Rowell, D. P., Kent, E. C., and Kaplan, A.: Global analyses of sea surface temperature, sea ice, and night marine air temperature since the late nineteenth century, Journal of Geophysical Research: Atmospheres, 108, 4407, https://doi.org/10.1029/2002JD002670, 2003.

Reithmeier, C. and Sausen, R.: ATTILA: atmospheric tracer transport in a Lagrangian model, Tellus B, 54, 278–299, https://doi.org/10.1034/j.1600-0889.2002.01236.x, 2002.

Roeckner, E., Bäumel, G., Bonaventura, L., Brokopf, R., Esch, M., Giorgetta, M., Hagemann, S., Kirchner, I., Kornblueh, L., Manzini, E., Rhodin, A., Schlese, U., Schulzweida, U., and Tompkins, A.: The Atmospheric General Circulation Model ECHAM5, Part I, Model Description, 2003.

845 Roeckner, E., Brokopf, R., Esch, M., Giorgetta, M., Hagemann, S., Kornblueh, L., Manzini, E., Schlese, U., and Schulzweida, U.: Sensitivity of Simulated Climate to Horizontal and Vertical Resolution in the ECHAM5 Atmosphere Model, Journal of Climate, 19, 3771–3791, https://doi.org/10.1175/JCLI3824.1, 2006.

Santee, M. L., Manney, G. L., Livesey, N. J., Schwartz, M. J., Neu, J. L., and Read, W. G.: A comprehensive overview of the climatological composition of the Asian summer monsoon anticyclone based on 10 years of Aura Microwave Limb Sounder measurements, Journal of

850 Geophysical Research: Atmospheres, pp. 5491–5514, https://doi.org/10.1002/2016JD026408, 2016JD026408, 2017.

Schulzweida, U.: CDO User Guide (Version 2.0.0), Zenodo, https://doi.org/10.5281/zenodo.5614769, 2021.

Siu, L. W. and Bowman, K. P.: Forcing of the Upper-Tropospheric Monsoon Anticyclones, Journal of the Atmospheric Sciences, 76, 1937 – 1954, https://doi.org/10.1175/JAS-D-18-0340.1, 2019.

Siu, L. W. and Bowman, K. P.: Unsteady Vortex Behavior in the Asian Monsoon Anticyclone, Journal of the Atmospheric Sciences, pp.

855 1–68, https://doi.org/10.1175/JAS-D-19-0349.1, 2020.

Smith, W. P., Pan, L. L., Honomichl, S. B., Chelpon, S. M., Ueyama, R., and Pfister, L.: Diagnostics of Convective Transport Over the Tropical Western Pacific From Trajectory Analyses, Journal of Geophysical Research: Atmospheres, 126, e2020JD034 341, https://doi.org/https://doi.org/10.1029/2020JD034341, e2020JD034341 2020JD034341, 2021.

Vogel, B., Günther, G., Müller, R., Grooß, J.-U., Hoor, P., Krämer, M., Müller, S., Zahn, A., and Riese, M.: Fast transport from Southeast

860 Asia boundary layer sources to northern Europe: rapid uplift in typhoons and eastward eddy shedding of the Asian monsoon anticyclone, Atmos. Chem. Phys., 14, 12 745–12 762, https://doi.org/10.5194/acp-14-12745-2014, 2014.

Vogel, B., Günther, G., Müller, R., Grooß, J.-U., and Riese, M.: Impact of different Asian source regions on the composition of the Asian monsoon anticyclone and of the extratropical lowermost stratosphere, Atmos. Chem. Phys., 15, 13 699–13 716, https://doi.org/10.5194/acp-15-13699-2015, 2015.

865 Vogel, B., Müller, R., Günther, G., Spang, R., Hanumanthu, S., Li, D., Riese, M., and Stiller, G. P.: Lagrangian simulations of the transport of young air masses to the top of the Asian monsoon anticyclone and into the tropical pipe, Atmospheric Chemistry and Physics, 19, 6007–6034, https://doi.org/10.5194/acp-19-6007-2019, 2019.

von Hobe, M., Ploeger, F., Konopka, P., Kloss, C., Ulanowski, A., Yushkov, V., Ravegnani, F., Volk, C. M., Pan, L. L., Honomichl, S. B., Tilmes, S., Kinnison, D. E., Garcia, R. R., and Wright, J. S.: Upward transport into and within the Asian monsoon anticyclone as inferred

870 from StratoClim trace gas observations, Atmospheric Chemistry and Physics, 21, 1267–1285, https://doi.org/10.5194/acp-21-1267-2021, 2021.

Wang, B. and LinHo: Rainy Season of the Asian–Pacific Summer Monsoon, Journal of Climate, 15, 386 – 398, https://doi.org/10.1175/1520-0442(2002)015<0386:RSOTAP>2.0.CO;2, 2002.

Wang, B., Jin, C., and Liu, J.: Understanding Future Change of Global Monsoons Projected by CMIP6 Models, Journal of Climate, 33, 6471

875 – 6489, https://doi.org/10.1175/JCLI-D-19-0993.1, 2020.

Wei, W., Zhang, R., Wen, M., Rong, X., and Li, T.: Impact of Indian summer monsoon on the South Asian High and its influence on summer rainfall over China, Clim. Dynam., 43, 1257–1269, https://doi.org/10.1007/s00382-013-1938-y, 2014.

Wei, W., Zhang, R., Wen, M., Kim, B.-J., and Nam, J.-C.: Interannual Variation of the South Asian High and Its Relation with Indian and East Asian Summer Monsoon Rainfall, J. Climate, 28, 2623–2634, https://doi.org/10.1175/JCLI-D-14-00454.1, 2015.

880 Winterstein, F. and Jöckel, P.: Methane chemistry in a nutshell – the new submodels CH4 (v1.0) and TRSYNC (v1.0) in MESSy (v2.54.0), Geoscientific Model Development, 14, 661–674, https://doi.org/10.5194/gmd-14-661-2021, 2021.

Wu, Y., Orbe, C., Tilmes, S., Abalos, M., and Wang, X.: Fast Transport Pathways Into the Northern Hemisphere Upper Troposphere and Lower Stratosphere During Northern Summer, Journal of Geophysical Research: Atmospheres, 125, e2019JD031552, https://doi.org/https://doi.org/10.1029/2019JD031552, e2019JD031552 10.1029/2019JD031552, 2020.

885 Yihui, D. and Chan, L. J. C.: The East Asian summer monsoon: an overview, Meteorol. Atmos. Phys., 89, 117–142, https://doi.org/10.1007/s00703-005-0125-z, 2005.

Zhang, Q., Wu, G., and Qian, Y.: The Bimodality of the 100 hPa South Asia High and its Relationship to the Climate Anomaly over East Asia in Summer, J. Meteorol. Soc. Jpn., 80, 733–744, https://doi.org/10.2151/jmsj.80.733, 2002.